

Rossby number regime, convection suppression, and dynamo-generated magnetism in inflated hot Jupiters

ALBERT ELIAS-LÓPEZ,^{1,2,3} MATTEO CANTIELLO,^{3,4} DANIELE VIGANÒ,^{5,2,6} FABIO DEL SORDO,^{7,8} SIMRANPREET KAUR,^{5,2}
AND CLÀUDIA SORIANO-GUERRERO^{5,2}

¹*Institut de Ciències de l'Espai (ICE-CSIC), Barcelona, Spain*

²*Institut d'Estudis Espacials de Catalunya (IEEC), Barcelona, Spain*

³*Center for Computational Astrophysics, Flatiron Institute, New York, USA*

⁴*Department of Astrophysical Sciences, Princeton University, New Jersey, USA*

⁵*Institut de Ciències de l'Espai (ICE-CSIC), Barcelona, Spain*

⁶*Institute of Applied Computing & Community Code (IAC³), Palma, Spain*

⁷*Scuola Normale Superiore, Piazza dei Cavalieri, Pisa, Italy*

⁸*INAF, Osservatorio Astrofisico di Catania, Catania, Italy*

ABSTRACT

Hot Jupiters (HJs) are commonly thought to host the strongest dynamo-generated magnetic fields among exoplanets, up to one order of magnitude larger than Jupiter. Thus, they have often been regarded as the most promising exoplanets to display magnetic star-planet interaction signals and magnetically-driven coherent radio emission, which unfortunately remains elusive, despite many diversified observational campaigns. In this work, we investigate the evolution of the internal convection and dynamo properties of HJs via one-dimensional models. We explore the dependency on orbital distance, planetary and stellar masses, and types of heat injection. We employ one-dimensional evolutionary models to obtain internal convective structures. Specifically, we obtain the Rossby number Ro as a function of planetary depth and orbital period, after showing that tidal synchronization is likely valid for all HJs. When the heat is applied uniformly, the convective layers of almost all HJs remain in the fast rotator regime, $Ro \lesssim 0.1$, except possibly the most massive planets with large orbital distances (but still tidally locked). We recover magnetic field strengths for inflated HJs by applying well-known scaling laws for fast rotators. When strong heat sources are applied mostly in the outer envelope and outside the dynamo region, as realistic Ohmic models predict, convection in the dynamo region often breaks down. Consequently, the heat flux and the derived surface magnetic fields can be greatly reduced to or below Jovian values, contrary to what is commonly assumed, thus negatively affecting estimates for coherent radio emission, and possibly explaining the failure in detecting it so far.

Keywords: convection - dynamo - magnetic fields - planets and satellites: interiors - planets and satellites: magnetic fields

1. INTRODUCTION

Hot Jupiters (HJs) are gaseous giant planets on close-in orbits, characterized by orbital periods of just a few days and separations $\lesssim 0.1$ AU (Fortney et al. 2021). Due to the proximity to their host stars, they are highly irradiated and tidally locked, with equilibrium temperatures up to 3000 K. This extreme external heating creates strong thermal gradients between their day and

night sides, driving strong atmospheric flows and equatorial zonal jets that shape their atmospheric dynamics (e.g., Showman & Guillot 2002; Showman et al. 2009; Heng & Showman 2015). Currently, several hundred HJs have been confirmed, enabling extensive population studies. One of the most intriguing findings is the so-called HJ radius anomaly (see Thorngren (2024) for a review), which remains one of the longest-standing open questions in exoplanetary science: observations show that HJs systematically exhibit inflated radii, significantly larger (up to twice the Jovian radius) than

those predicted by standard evolutionary models. There is a clear trend between the degree of radius inflation and stellar irradiation, once the planetary equilibrium temperature exceeds $T_{\text{eq}} \gtrsim 1000$ K (Weiss et al. 2013), a fundamental hint to the underlying physical mechanism. However, the irradiation alone can contribute to radius inflation only up to approximately $\sim 1.3 R_J$ at Gyr ages, depending also on the mass and the amount of heavy elements (Guillot et al. 1996; Guillot & Showman 2002; Arras & Bildsten 2006; Burrows et al. 2007; Fortney et al. 2007). Several mechanisms have been proposed to delay the shrinking and cooling (Spiegel & Burrows 2013; Thorngren 2024): enhanced opacities (Burrows et al. 2007), inhibition of large-scale convection (Chabrier & Baraffe 2007), hydrodynamic effects leading to dissipation in deep layers (Showman & Guillot 2002; Showman et al. 2009; Li & Goodman 2010; Youdin & Mitchell 2010), and Ohmic dissipation of atmospherically induced magnetic field. Among these proposed mechanisms, the latter has received considerable attention, with several quantitative studies (e.g., Batygin & Stevenson 2010; Batygin et al. 2011; Perna et al. 2010a; Wu & Lithwick 2013; Ginzburg & Sari 2016; Knierim et al. 2022; Soriano-Guerrero et al. 2023, 2025; Viganò et al. 2025). But multiple mechanisms may operate simultaneously (Sarkis et al. 2021).

One of the most elusive characteristics of exoplanets is their magnetism. Observational estimates of magnetic fields in some HJs, with considerable uncertainties, have been proposed so far in very few works, via star-planet interaction (SPI) models, used to interpret the observed trends of X-ray luminosities vs presence of short-orbit planets (Scharf 2010), or the modulation of Ca II K lines with HJ orbital periods (Cauley et al. 2019). Self-sustained dynamo simulations for the planetary scenario have been used to derive scaling laws that relate various dimensionless parameters (Christensen & Aubert 2006; Yadav et al. 2013), which have been validated by the comparison with the observed magnetic fields on Earth, Jupiter, and in fast-rotating low-mass stars (Christensen et al. 2009; Reiners & Christensen 2010). These scaling laws state that, in the fast rotator regime, convective heat flux determines the magnetic field strength. When applied in the HJ context, heat-flux scaling laws generally found an increase by up to ~ 1 order of magnitude of the inferred magnetic fields compared to non-inflated gas giants, if the extra heat needed to explain the inflation is assumed to take the role of the heat convective flux in the scaling laws (Yadav & Thorngren 2017; Kilmatis et al. 2024). Note that, on the contrary, slowly rotating cool stars observationally show a correlation of the magnetic activity indicators with the rotation rate (Reiners

et al. 2014). The transition from a rotation-dominated (slow rotators) to a convective-heat-flux-dominated (fast rotators) dynamo strength is seen to be fairly sharply defined by the Rossby number $\text{Ro} \sim 0.12$. In this sense, planetary scaling laws applicable to slow rotators assumed a proportionality with the rotation rate rather than the heat flux (e.g., Sánchez-Lavega 2004; Stevens 2005). A primary aim of this work is to shed light on which regime applies to HJs, considering the observed range of their relevant parameters: planetary mass, stellar type, and star-planet separation.

Moreover, since virtually all the existing scaling laws predict a correlation between magnetic field intensity and planetary mass, giant exoplanets, and HJs in particular, have been historically considered the main candidates for the still elusive quest of Jovian-like coherent radio emission (e.g., de Gasperin et al. 2020; Narang et al. 2024 and references within), in the form of electron cyclotron maser (Dulk 1985). The latter has been detected from all magnetized planets in the solar system (Zarka 1998), but can be detected from the ground only if the cyclotron frequency (ECM), $\nu_c \simeq 2.8 B$ [G] MHz, is larger than the ~ 10 MHz ionospheric cut-off. This implies that, to be detected by ground-based radio interferometers, the magnetic field needs to be at least as intense as the Jovian one. In this sense, the second main aim of this work is to explore the trends of the estimates of magnetic field intensity at the dynamo region and the planetary surface, considering their Rossby regime and applying the appropriate scaling law at a given age, with the internal structure and (convective) luminosity given by long-term evolutionary models. Understanding the magneto-thermal dependence on orbital distance and age can help guide future observations toward the most promising targets.

This work is organized as follows. In Sect. 2 we summarize the values of irradiation and tidal locking timescales, based on the HJ population. Sect. 3 introduces the evolutionary models and the amount of additional internal heat as a function of irradiation, based on the statistical study by Thorngren & Fortney (2018). We also discuss how the injection and irradiation affect the internal convective layers. In Sect. 4, we obtain internal profiles of the local Rossby number and discuss how it depends on age, star-planet separation, planetary mass, and stellar type. In Sect. 5 we estimate the dynamo-generated magnetic fields, and the corresponding values at the planetary surfaces, via the scaling laws mentioned above. We also discuss the related implications for magnetic SPI and ECM radio emission. Finally, we highlight the main conclusions in Sect. 6.

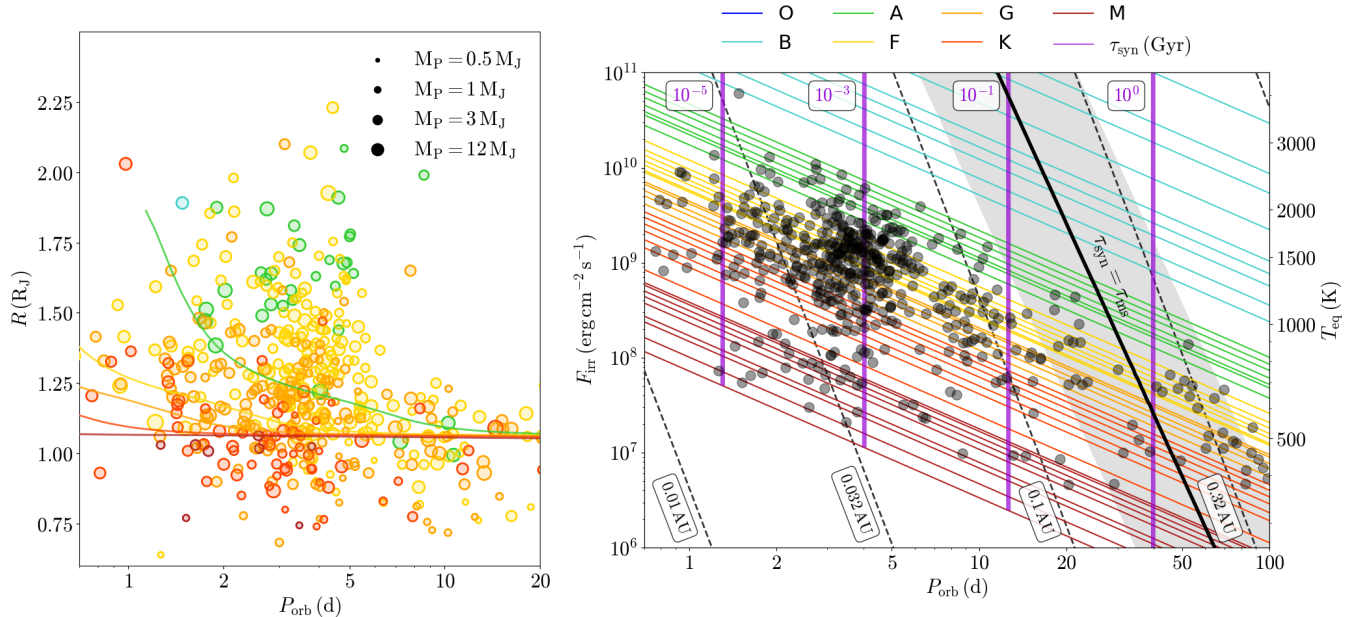


Figure 1. Population properties for the confirmed gas giant exoplanet population with mass $M_P > 0.2 M_J$, considering the host star effective temperature and radius to obtain the irradiation flux F_{irr} , and the corresponding equilibrium temperature T_{eq} . Data is extracted from the NASA exoplanet archive^a (Christiansen et al. 2025). Colors indicate the main-sequence stellar type of the host star. Errors are not shown, for the sake of visibility. *Left:* planetary radius as a function of orbital period. Marker size denotes the planetary mass. *Right:* F_{irr} as a function of planetary orbital period for the same exoplanetary systems. The dashed black lines mark constant separation a . The purple vertical lines correspond to different synchronization timescales, τ_{syn} in Gyr, obtained with Eq. 4, assuming $M_P = 1 M_J$, $Q'_P = 5 \cdot 10^5$, $\alpha = 2/5$, and $\omega_i = 2\pi/5 \text{ h}^{-1}$ (see text). The solid black line indicates where the main-sequence lifetime equals the synchronization timescale.

^a<https://exoplanetarchive.ipac.caltech.edu/>

2. IRRADIATION AND TIDAL SYNCHRONIZATION

The irradiation flux received by a planet in a specific circular orbit of radius a (hereafter, separation) around its host star is:

$$F_{\text{irr}} = \frac{L_\star}{4\pi a^2} = \sigma_{\text{SB}} T_{\text{eff}}^4 \frac{R_\star^2}{a^2}, \quad (1)$$

where R_\star , L_\star and T_{eff} are the stellar radius, luminosity and effective temperature, respectively. Stellar luminosities are taken from tabulated main-sequence star values⁹ (i.e., obtained from mass-luminosity relations, $L \propto M^a$, where a depends on stellar mass). The resulting irradiation fluxes for HJs typically range from 10^8 to $10^{10} \text{ erg cm}^{-2} \text{ s}^{-1}$, orders of magnitude larger than the fluxes reaching Earth and Jupiter ($1.4 \cdot 10^6$ and $5 \cdot 10^4 \text{ erg cm}^{-2} \text{ s}^{-1}$, respectively). The corresponding

planetary equilibrium temperature is:

$$T_{\text{eq}} = \left(\frac{F_{\text{irr}}(1 - A_B)}{4\sigma_{\text{SB}}} \right)^{1/4} = (1 - A_B)^{1/4} \left(\frac{R_\star}{2a} \right)^{1/2} T_{\text{eff}}, \quad (2)$$

where A_B is the planetary albedo (which we consider zero for simplicity) and σ_{SB} is the Stefan-Boltzmann constant.

The left panel of Fig. 1 shows planetary radii, R_P , as a function of the orbital period P_{orb} for the currently known HJ population with masses $M_P > 0.2 M_J$. In the right panel, we also show the irradiation flux F_{irr} and equilibrium temperature T_{eq} , as a function of P_{orb} , for the same HJ population. Colors correspond to the spectral type of the host star. The bulk of known HJs orbit F, G, and K-type stars, with orbital distances lower than 0.1 AU, i.e. periods $P_{\text{orb}} \lesssim 10$ days. The lines in the left panel correspond to the radii of standard planetary evolutionary models with $1 M_J$ masses, at 5 Gyr, considering only irradiation and no internal extra heat injection (see Sect. 3.1) around different stars (see Table 1 for details). Note that most planets are above these lines, showing signs of inflation and the need for a heat injection mechanism. The HJ population below these lines

⁹ In this work, we use the tables of <https://sites.uni.edu/morgans/astro/course/Notes/section2/spectralmasses.html>

is mostly small planets compatible with high metallicities or large rocky cores (Laughlin et al. 2011), possibly related to early severe mass losses (Sestovic et al. 2018; Lazovik 2023), which are factors that we do not consider for our evolutionary models, since we aim at studying the average properties of HJs, i.e. with inflated radii. Note that, as mentioned before, the clear correlation is between R_P and F_{irr} (or T_{eq}). However, as we use P_{orb} to define the Rossby number and dynamo regime (see Sect. 4), we choose it as a key variable, instead of the stellar irradiation F_{irr} . Due to the degeneracy between stellar mass and P_{orb} in defining F_{irr} , the correlation R_P vs P_{orb} (left panel) is essentially lost, in agreement with e.g. Weiss et al. (2013).

Observed HJs are commonly seen to sit on low-eccentricity orbits (Zink & Howard 2023), and assumed to be tidally locked, meaning that their rotational and orbital periods P_{orb} are identical. Secondary transits finding azimuthal displacements of the hottest points compared to the substellar points to the East (e.g. Knutson et al. 2007) or West (e.g. Dang et al. 2018), are usually interpreted in terms of atmospheric circulation effects, rather than a deviation from the tidal locking regime. Here, we revisit with some detail the quantitative assessment of the timescale τ_{syn} required to achieve tidal synchronization, by calculating the rate of change of the planetary rotation ω under the assumption of circular orbits and zero obliquity:

$$\frac{d\omega}{dt} = \frac{9}{4} \frac{1}{\alpha Q'_P} \frac{GM_P}{R_P^3} \left(\frac{M_*}{M_P}\right)^2 \left(\frac{R_P}{a}\right)^6 \quad (3)$$

where $\alpha = \frac{I}{M_P R_P^2}$, $Q'_P = \frac{3Q_P}{2k_{2,P}}$,

M_P and R_P are the planetary mass and radius, respectively, I is the planetary moment of inertia, Q_P is the dissipation factor, $k_{2,P}$ is the Love number of the planet and G is the gravitational constant (e.g. Goldreich & Soter 1966; Murray & Dermott 1999; Grießmeier et al. 2007). The synchronization timescale is then given by:

$$\tau_{\text{syn}} \approx \frac{\Delta\omega}{d\omega/dt} = \frac{4}{9} \frac{d^6 I Q'_P \Delta\omega}{GM_*^2 R_P^5} \simeq \frac{G\alpha}{36\pi^4} \frac{M_P Q'_P P^4 \omega_i}{R_P^3}, \quad (4)$$

where P is the orbital period, and $\Delta\omega = \omega_i - \omega_f \sim \omega_i$, since $\omega_i \gg \omega_f$, the difference between initial and final rotation. On the right panel of Fig. 1 we show in purple different lines of constant τ_{syn} for a $M_P = 1 M_J$ planet, assuming $\alpha = 2/5$ (homogeneous sphere), $R_P = 1.5 R_J$, $Q'_P = 5 \cdot 10^5$ as in Grießmeier et al. (2007), and an initial spin period of 5 hours typical of known fast-rotating substellar objects, $\omega_i = (2\pi/5 \text{ h})$, and conservatively larger than the breakup values which can be used as initial con-

dition (Batygin 2018). Most of the parameters adopted in the above expression evolve significantly over time, particularly at early stages ($t \lesssim 10 \text{ Myr}$) when planetary contraction proceeds rapidly, and orbital migration as well as interactions with the protoplanetary disk are important. For this reason, we adopted reference values that yield systematically conservative estimates, overestimating τ_{syn} by factors of a few. Specifically, realistic adjustments would include considering a radially dependent density profile (moment of inertia factor $\alpha < 2/5$), larger radii of very young gas giants depending on their formation entropy (e.g., Fortney et al. 2007), and shorter initial spin periods, which can be as brief as about 2 hours for newborn brown dwarfs and low-mass stars.

We show in Fig. 1 the location where τ_{syn} equals the main sequence lifetime of the host star as a black line. We calculated the duration of the main sequence as $\tau_{\text{ms}} = 10 \text{ Gyr} (M_*/M_\odot)^{-2/5}$ (Carroll & Ostlie 2017, chap. 13). Planets lying to the left of this line are expected to be tidally locked, or to reach that state within the stellar lifetime. To evaluate how planetary mass affects τ_{syn} , we observe that for a $0.2 M_J$, $2 R_J$ planet, τ_{syn} becomes a factor of 10 smaller. On the other hand, a massive $M_P = 10 M_J$ takes about one order of magnitude longer to synchronize. This range of values is shown by the gray shading around the $\tau_{\text{syn}} = \tau_{\text{ms}}$ (and each τ_{syn} line has a similar uncertainty). From Fig. 1, it is clear that the HJs population with $T_{\text{eq}} > 1000 \text{ K}$ should be tidally locked, and only warm Jupiters (having $P_{\text{orb}} \gtrsim 20 - 30 \text{ d}$) could still preserve their initial faster rotation.

Note that, recently, Wazny & Menou (2025) used global circulation models to show that the presence of a non-negligible magnetic torque in atmospheres permeated by thermally driven winds could lead to substantial spin-orbit asynchronization, particularly in planets with high equilibrium temperatures and strong magnetic fields. These effects are beyond the scope of this paper, and thus, we adopt the assumption of tidal synchronization throughout our analysis.

3. PLANETARY EVOLUTION

3.1. Cooling model

We use the public code MESA¹⁰ (Paxton et al. 2011, 2013, 2015, 2018, 2019; Jermyn et al. 2023), specifically its version 24.08.1, to evolve irradiated gas giants, allowing for additional internal heat deposition. The code solves the time-dependent one-dimensional stellar structure equations, using the adapted module for gas giants

¹⁰ <https://mesastar.org/>

(Paxton et al. 2013). The set of equations includes mass conservation, hydrostatic equilibrium, energy conservation, and energy transport:

$$\frac{dm}{dr} = 4\pi r^2 \rho, \quad (5)$$

$$\frac{dP}{dm} = -\frac{Gm}{4\pi r^4}, \quad (6)$$

$$\frac{dL}{dm} = -T \frac{ds}{dt} + \epsilon_{\text{irr}} + \epsilon_{\text{heat}}, \quad (7)$$

$$\frac{dT}{dm} = -\frac{GmT}{4\pi r^4 P} \nabla, \quad (8)$$

where m is the mass enclosed within a radius r , ρ is the density, P is the pressure, G the gravitational constant, s the specific entropy, T the temperature, L the internal luminosity, and $\nabla \equiv d \ln T / d \ln P$ is the logarithmic temperature gradient, which is set to the smallest between the adiabatic gradient and the radiative gradient. The right-hand side of the energy equation (7) includes the specific heating/cooling rates: gravitational contraction, stellar irradiation ϵ_{irr} (Guillot et al. 1996), and any internal heat source ϵ_{heat} . The latter has been included in several previous works using MESA, to consider the effect of continuous heat deposition and inflation in HJs (Komacek & Youdin 2017; Thorngren & Fortney 2018; Komacek et al. 2020). The set of equations is closed using the MESA equation of state (Paxton et al. 2019), which, for the gas giant ranges of interest, is essentially the interpolation of the Saumon et al. (1995) equation of state for H-He mixtures.

The atmospheric irradiation is implemented in a simplified way, as in previous MESA HJ works (Paxton et al. 2013; Komacek & Youdin 2017; Komacek et al. 2020): the specific energy absorption rate is assumed to be $\epsilon_{\text{irr}} = F_{\text{irr}} / (4\Sigma_*)$, i.e. a uniform deposition of heat through the outermost mass column $m(r) \leq \Sigma_*$, where Σ_* parametrises how deep is the column which atmospheric absorption occurs, without a more detailed modeling of the atmospheric composition and opacities. We fix it to 200 g cm^{-2} , which approximately corresponds to a grey opacity $\kappa = 5 \times 10^{-3} \text{ cm}^2 \text{ g}^{-1}$, with a maximum depth of a fraction of a bar. We consider a constant-in-time value of the stellar irradiation F_{irr} , thus neglecting the slight increase in stellar luminosity $L_*(t)$ throughout the main sequence phase. We refer to Lopez & Fortney (2016); Komacek et al. (2020) for works including this effect, important especially at the end of the main sequence and beyond it. As commonly done in similar previous works, we assume here an inert homogeneous rocky core of mass $10 M_{\oplus}$ and homogeneous density $\rho_c = 10 \text{ g cm}^{-3}$ (which together set the core size R_{core}), and a fixed solar composition for the envelope. We don't discuss here the effects of the total metallicity,

Table 1. Characteristics of the stars considered throughout the text (specifically the planetary irradiated models in Fig. 1 and in App. A.

Stellar type	T_* [K]	L_* [L_{\odot}]	M_* [M_{\odot}]
AV3	8750	12	1.86
FV5	6700	2.4	1.25
GV2	5800	1	1.00
KV3	4800	0.31	0.746
MV3	3500	0.046	0.463

and the comparison between a diluted or solid core, since they have been shown in detailed cooling studies for HJs (e.g., Burrows et al. 2007; Thorngren et al. 2016) and Solar planets (e.g., Wahl et al. 2017; Yıldız et al. 2024).

Generally speaking, during the initial stages ($t \lesssim 10$ Myr), the evolution of the planetary radius depends on the assumed initial condition (i.e., the internal entropy at formation). At later times, instead, models are insensitive to it, and the planet shrinks during its long-term evolution due to its cooling (e.g. Burrows et al. 2007; Paxton et al. 2013). Therefore, the detailed value of the initial condition is not relevant. To help MESA numerical convergence at early ages for extremely irradiated models, we also use a short relaxation phase at the beginning of evolution, after applying the irradiation.

We denote the depth at which irradiation reaches R_{irr} , and the radiative-convective boundary as R_{RCB} . We also define the outer radius of the dynamo region, R_{dyn} , by the pressure above which hydrogen becomes metallic, which we take as $P_{\text{dyn}} = 1 \text{ Mbar}$ (French et al. 2012). Note that, strictly speaking, the transition to the metallic hydrogen is not sharp and depends on the temperature, as well (Bonitz et al. 2024). However, for simplicity, and given the high theoretical uncertainties about the exact location of the phase transition, we consider a single value of P_{dyn} as a first approximation. In the metallic hydrogen region, the electrical conductivity is $\sigma \sim 10^6 \text{ S m}^{-1}$ (French et al. 2012; Bonitz et al. 2024), orders of magnitude larger than in the molecule-dominated envelope, where the conductivity is dominated by the thermal ionization of alkali metals (e.g., Kumar et al. 2021). Considering a typical convective velocity $v_{\text{conv}} \sim 0.1 \text{ m s}^{-1}$ (Fuentes et al. 2023), a Jupiter-like shell thickness $L \sim 5 \cdot 10^7 \text{ m}$, the resulting magnetic Reynolds number in the dynamo region is $\text{Rm} = v_{\text{conv}} L / \eta = \mu_0 \sigma v_{\text{conv}} L \sim 10^6 - 10^7$ (where η is the magnetic diffusivity and μ_0 is the magnetic permeability in vacuum), well above the minimum values commonly thought to be needed for dynamo, $\text{Rm} \gtrsim 50$ (Christensen & Aubert 2006).

Hereafter, we consider planets with $1 \text{ d} \lesssim P_{\text{orb}} \lesssim 30 \text{ d}$ orbiting a representative sample of five main-sequence stars, listed in Table 1. We test planetary masses from 0.5 to $12 M_{\text{J}}$, sampling the whole inflated HJ population in period and flux as seen on the right of Fig. 1. We restrict to planets $M_{\text{P}} \geq 0.5 M_{\text{J}}$ due to the above-mentioned contamination of partially evaporated, high-metallicity planets, as discussed also in e.g. Sestovic et al. (2018).

3.2. Extra heat

Since the radius inflation, which calls for continuous internal heat deposition, correlates with the irradiation flux (Weiss et al. 2013), a commonly used parameter is the heating efficiency ϵ , defined as the ratio between the total deposited heat rate, $Q_{\text{dep}} = \int_M \epsilon_{\text{heat}} dm$, and the irradiation flux integrated over the planetary surface:

$$\epsilon = \frac{Q_{\text{dep}}}{\pi R^2 F_{\text{irr}}} . \quad (9)$$

Values of efficiency of a few percent or less are enough to inflate planets to the observed radii, if the heat is deposited in the convection region (e.g. Batygin & Stevenson 2010; Batygin et al. 2011; Wu & Lithwick 2013; Komacek & Youdin 2017). A detailed statistical study by Thorngren & Fortney (2018) derived an analytical expression for the amount of deposited heat fraction as a function of the incident flux, $\epsilon(F_{\text{irr}})$, that best fits the trend $R_{\text{P}}(F_{\text{irr}})$ seen in the entire HJ population:

$$\epsilon = (2.37^{+1.3}_{-0.26} \%) \exp \left[- \frac{(\log_{10}(F_{\text{irr}}/F_0) - 0.14^{+0.060}_{-0.069})^2}{2 \cdot (0.37^{+0.038}_{-0.059})^2} \right] , \quad (10)$$

where $F_0 = 10^9 \text{ erg s}^{-1} \text{ cm}^{-2}$. This inferred efficiency shows a strong, non-monotonic dependence on the stellar irradiation: the maximum heating efficiency grows with T_{eq} to reach a maximum of $\sim 2.5\%$ at $T_{\text{eq}} \approx 1500 \text{ K}$ and then decreases, having $\sim 0.2\%$ at $T_{\text{eq}} \approx 2500 \text{ K}$. Such a non-monotonic trend fits very well with the Ohmic models, for which, as the induced field increases with T_{eq} , the Lorentz forces exert an effective larger drag on the thermal winds (e.g., Perna et al. 2010b; Menou 2012). As a consequence, very hot Jupiters might have slower winds, which limit the available energy for the magnetic induction and decrease the overall heating efficiency.

Note that the expression above is purely phenomenological and shows high standard deviations, reflecting the large HJ radius dispersion at a given T_{eq} . In a similar work, Sarkis et al. (2021) obtain a similar fit with a Gaussian function for the flux, but with the efficiency

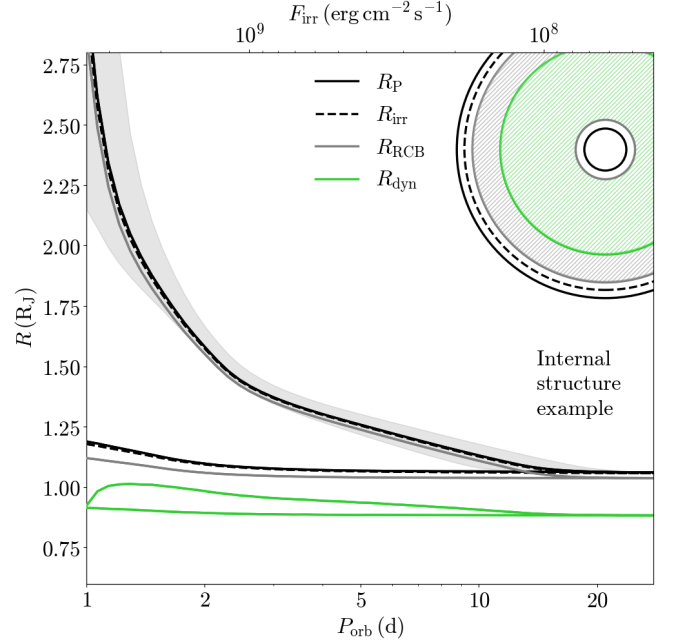


Figure 2. Dynamo outer surface radius R_{dyn} (green), RCB radius R_{rcb} (gray), bottom of the irradiated region R_{irr} (dashed), and planetary radius R_{P} (solid black), for a $1 M_{\text{J}}$ planet orbiting a $1 M_{\odot}$ star, at 5 Gyr, as a function of orbital period, for both heated (upper lines) and non-heated models (lower lines). The gray area shows the outer radius uncertainty for the heated models, accounting for the range of parameters quoted in Eq. (10). In the upper right corner, we show a sketch of the relative position, not at scale, of the different radii, including the internal core R_{core} (solid black) and a possible stratified layer close to the core (gray).

peaking at $T_{\text{eq}} \approx 1850 \text{ K}$. Moreover, both Thorngren & Fortney (2018) and Sarkis et al. (2021) note that this heating efficiency is degenerate with heavy mass fraction. Despite these uncertainties and caveats, the analytical function above, which we use in this study, offers an easy way to explore the representative internal heating we can infer for a given planet and star.

The efficiency is not the only parameter to consider: it is also important to specify where the heat is deposited, i.e., the $\epsilon_{\text{heat}}(r)$ profile (Ginzburg & Sari 2015; Komacek & Youdin 2017). Since we are not assuming any particular mechanism responsible for the extra heat, for simplicity we inject a uniform specific heat rate, $\epsilon_{\text{heat}} = Q_{\text{dep}}/M_{\text{shell}}$ (heat per unit time per unit mass), over a given shell with mass M_{shell} , delimited by two radii, r_{bot} and r_{top} , for which we consider two simple scenarios:

1. Extended deposition in the dynamo region ($\epsilon_{\text{heat,extended}}$): $r_{\text{bot}} = R_{\text{core}}$; $r_{\text{top}} = R_{\text{dyn}}$.

2. Deposition in the outer convective region, outside the dynamo region ($\epsilon_{\text{heat,outer}}$): $r_{\text{bot}} = R_{\text{dyn}}$; $r_{\text{top}} = R_{\text{irr}}$.

Note that if one considers heating up to the irradiated layer ($r_{\text{bot}} = R_{\text{core}}$; $r_{\text{top}} = R_{\text{irr}}$), i.e. including part of the stratified, radiative layers, the results are almost indistinguishable results from the first one. As noted in previous works (Komacek & Youdin 2017), heating the radiative region is less effective in terms of inflated radii, because the mass in the radiative region is very small and the heat mostly escapes outward. Moreover, for very high values of irradiation and heating, including the outermost layers, the code can fail to converge more easily.

The second type of heating injection (i.e., above the dynamo radius) is inspired by the fact that most heating mechanisms deposit the bulk of energy in low-density regions. Physical models such as ohmic, tidal, or turbulent heating have different heating distributions (Batygin & Stevenson 2010; Batygin et al. 2011; Wu & Lithwick 2013; Ginzburg & Sari 2015, 2016), but all of them deposit most of the heat in the outer layers of the planet, well outside the metallic dynamo region.

As we will show in the Sect. 3.4 and below, heat deposition above the dynamo region leads to significant differences. Further exploration of the heating radial profile has been conducted in detail in several other works, e.g. different power laws (Ginzburg & Sari 2015), or Gaussian profiles at different depths (Komacek & Youdin 2017; Komacek et al. 2020), and is not a matter of this study, where we only consider the two simplified scenarios above.

3.3. Extended heat cases: general properties

In Fig. 2 we show the evolution of the planetary radius of a $1 M_{\text{J}}$ planet orbiting a $1 M_{\odot}$ star at 5 Gyr, as a function of the orbital period. In the plot, we compare irradiated models and heated models with the extended type of injection. Planets heated as shown in Eq. (10) (Thorngren & Fortney 2018) inflate considerably and reach the range of observed HJ radii. The uncertainty for the outer radius of internally heated models reflects different values for $\epsilon_{\text{heat}}(F_{\text{irr}})$, considering the uncertainty ranges of the parameters in Eq. (10). We also show a not-to-scale sketch of the different radii for illustration purposes. The order $R_{\text{P}} > R_{\text{irr}} > R_{\text{RCB}} > R_{\text{dyn}}$ always holds for both heated and non-heated models. There is only an exception for the highest irradiated cases, in which an additional convective outer layer above R_{irr} appears. More considerations regarding the behavior of convective regions for highly irradiated and heated models are found below.

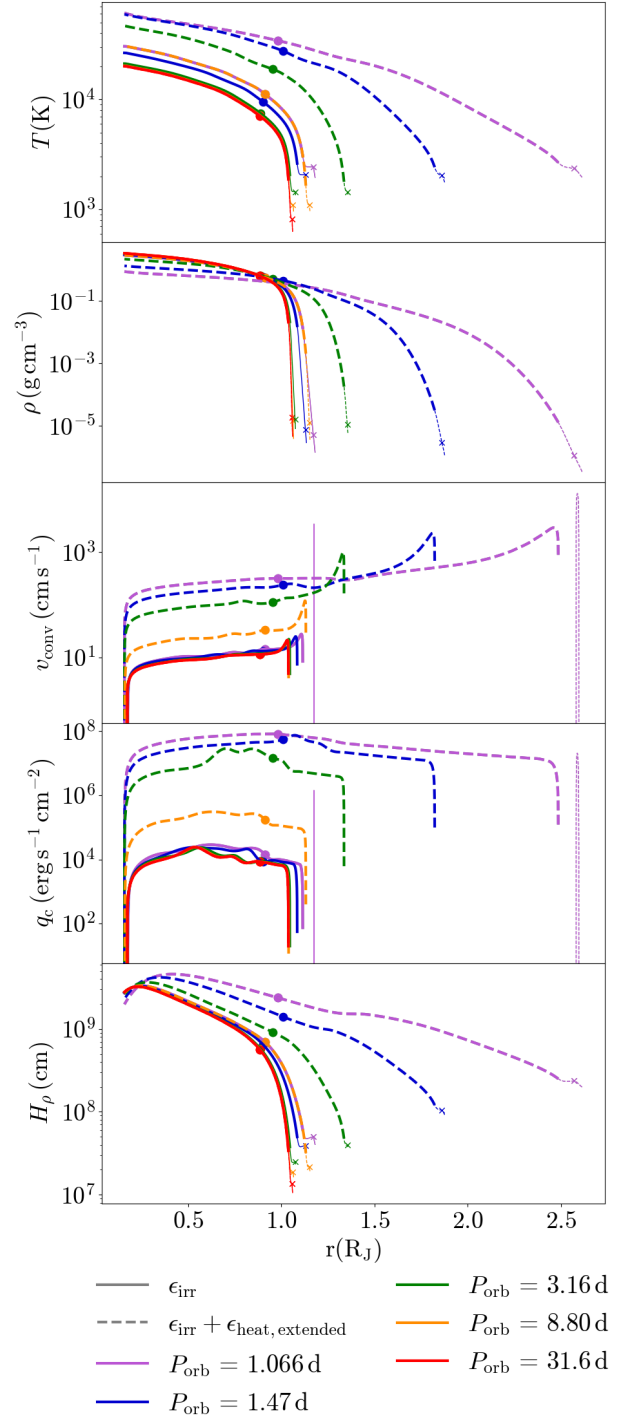


Figure 3. Radial profiles of temperature, density, convective velocity, heat convective flux, and density scale height, for $1 M_{\text{J}}$ planets orbiting a $1 M_{\odot}$ star at 5 Gyr with different P_{orb} . Models without and with extra heating (below R_{dyn}) are shown by solid and dashed lines, respectively. R_{irr} is marked with a cross, R_{RCB} is the transition from thick to thin lines, and R_{dyn} is marked with a dot.

In Fig. 3 we show the internal profiles for some chosen periods in Fig. 2. Specifically, we show the temperature T , the density ρ the density scale height $H_\rho(r) = P/\rho g$, the convective velocity v_{conv} , and the convective flux q_c . The convective velocity comes from mixing length theory (MLT) based on the model in Kuhfuss (1986), which reduces to the expression given by (Cox & Giuli 1968, chap. 14), in the limit of long time steps (see Paxton et al. (2011); Jermyn et al. (2023) for details). We define q_c as the convective heat flux in the dynamo-generating region as follows:

$$q_c = \frac{2 c_P T \rho^2 v_{\text{conv}}^3}{P \delta}, \quad (11)$$

where $\delta = -(\partial \ln \rho / \partial \ln T)_P$.

When the planets are far from the heating efficiency peak, there is almost no difference between heated and non-heated models. Instead, inflation implies very different radial profiles: T , H_ρ , v_{conv} , and q_c substantially increase for a given model and age, while the density in the innermost parts decreases due to the higher internal temperature (i.e., inflation and smaller mass/volume ratio).

Note that we analyze models at 5 Gyr, which are representative of the bulk of HJs. Most evolution models of irradiated, internally heated HJs show that at \sim Gyr ages (corresponding to the vast majority of known HJs), the shrinking and cooling stalls, due to the essential balance between the internal heating and the long-term cooling (e.g., Komacek & Youdin 2017). Therefore, the internal structure doesn't change notably. In reality, this behaviour relies on the assumption that both the stellar luminosity and the internal heat are constant in time, then neglecting the evolution of stellar luminosity (see Lopez & Fortney 2016; Komacek et al. 2020 for studies of re-inflation in this context), and the possible change in the heating efficiency of the underlying mechanism (see Viganò et al. (2025) for Ohmic models with evolving heating rates).

3.4. Heat deposited in the outer region: suppression of convection

Substantial differences appear with the outer type of heat injection. The heat is deposited in a significantly shallower layer, which, for a high enough deposited heat rate, leads to internal convection suppression. This is physically justified by comparing the logarithmic temperature radiative gradient ($\nabla_{\text{rad}} = 3\kappa LP/64\pi\sigma GmT^4$) and convective/adiabatic gradient (∇_{ad}), which MESA determines using MLT. Following the Schwarzschild criterion, the actual temperature gradient ∇ is set to the smaller of the adiabatic or radiative, i.e., $\nabla =$

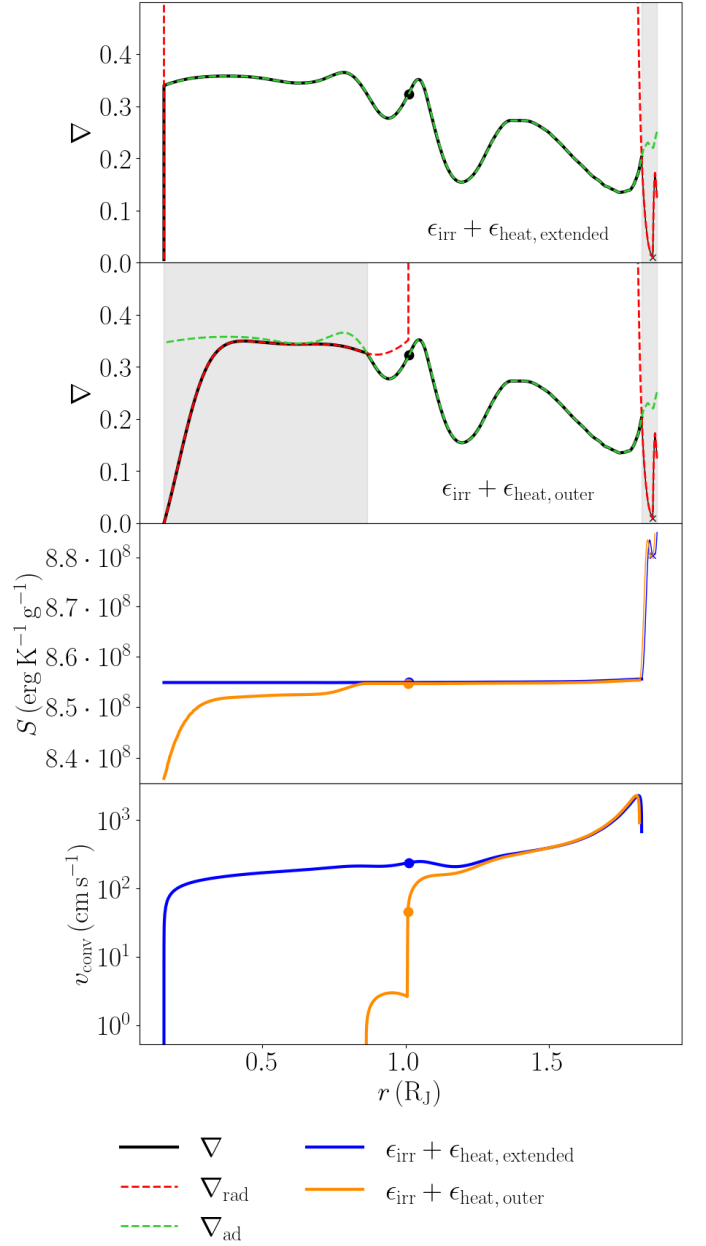


Figure 4. Radial profiles of extended and outer heating models for a $1 M_J$ planet orbiting a $1 M_\odot$ star at 5 Gyr, with $P_{\text{orb}} = 1.47$ d. *Top panels:* Total logarithmic temperature gradient ∇ (black solid line), with the adiabatic (green dashed line) and radiative (red dashed line) temperature gradients, ∇_{ad} and ∇_{rad} , respectively. Gray zones mark stably stratified layers, i.e., $\nabla_{\text{rad}} < \nabla_{\text{ad}}$. *Bottom panels:* Specific entropy and convective velocity for the same models.

$d \ln T / d \ln P = \min(\nabla_{\text{rad}}, \nabla_{\text{ad}})$. Therefore, convection develops where ∇_{ad} is lower than ∇_{rad} , and on the other hand, the stably stratified layers arise when ∇_{rad} is lower than ∇_{ad} . Similar to Komacek & Youdin (2017), we plot ∇ , ∇_{rad} and ∇_{ad} in the two top panels of Fig. 4 for the

same 1 M_J planet with a $P_{\text{orb}} = 1.47$ d. The gradient inversion is always present in the outermost part of the planets, covering at least the irradiation depth. For the model with outer heating, the inversion also happens in a substantial part of the interior near the core, creating an additional internal stratified layer.

This behavior can also be seen with the specific entropy gradient: the extended heated model (blue lines) remains isentropic over a large volume, whereas the outer heating model produces a positive entropy gradient in correspondence with the layers just below where the heat is deposited. With the outer heating case, v_{conv} , and thus q_c , greatly reduces and even vanishes below R_{dyn} . The reduction of convective region size has been briefly mentioned in previous works where intense heating was deposited at specific interior locations (e.g., Komacek & Youdin 2017; Komacek et al. 2020). Importantly, it has relevant consequences for the internal dynamo (see Sect. 5.1).

Note that, on the contrary, planetary radius, external luminosity (set by R_P and F_{irr}), and the profiles of T , ρ , P , g are almost indistinguishable between the two heating types. This is because the layers responsive to heating are the external ones, due to their lower density. They are the ones responsible for the inflation, as seen by comparing how the density profiles extend, in Fig. 3. Therefore, depositing the heat over most of the planet, or only in the outer convective region, provides a very similar evolution of thermodynamic profiles.

Additionally, in the most irradiated models, a shallow convective layer arises in the outermost regions of the planet. HJ shallow layer is conductive due to alkali thermal ionization (Kumar et al. 2021) and thus could be potentially an additional source of convective dynamo. However, note that the convection is suppressed if the internally generated magnetic field is strong enough, higher than the critical value, $B_{\text{crit, r}}$, given by (Jermyn & Cantiello 2020, Eq. 9). Among the models shown in Fig. 3, only the extremely irradiated case with $P_{\text{orb}} \simeq 1$ d shows this shallow convective outer layer, as seen in both v_{conv} and q_c panels. Its associated $B_{\text{crit, r}}$ corresponds to about 100 G, which, as we will see in Sect. 5.1, is higher than the values that we estimate, therefore leaving open the possibility of such an additional convective layer. However, note that these results are sensitive to external boundary conditions and the heat deposition $\epsilon_{\text{irr}}(P)$. Furthermore, the surface deposition for HJs is far from uniform, which would lead to a stronger convection layer in the dayside and hamper its existence in the nightside. Global circulation three-dimensional models are needed to address the possible existence of such a layer and their interaction with the thermal winds.

4. ROSSBY NUMBER ESTIMATION

The Rossby number, Ro , is the ratio between inertial forces (dominated by convection) and the Coriolis force. Most planets in the solar system are fast rotators, i.e. they are in a low Ro regime: defining $Ro = P_{\text{rot}}/\tau_{\text{turn}}$, i.e., the ratio of rotation period to convection turnover timescales, Earth and Jupiter have $Ro \sim 10^{-5}$ and 10^{-4} , respectively. In this regime, the widely used dynamo scaling laws by Christensen et al. (2009), explained below, apply. In HJs, as seen in Sect. 2, tidal locking implies $P_{\text{rot}} = P_{\text{orb}}$. We obtain the convective timescale, $\tau_{\text{turn}}(r)$, from the evolutionary models, by using the radial profiles of density scale height, $H_\rho(r)$, and convective velocity, $v_{\text{conv}}(r)$, so that

$$Ro(r) = \frac{P_{\text{orb}} v_{\text{conv}}(r)}{H_\rho(r)}. \quad (12)$$

In Fig. 5 we show $Ro(r)$, for 50 different values of $P_{\text{orb}} \in [1, 25]$ d, considering the representative case of a 1 M_J orbiting a 1 M_\odot star, at 5 Gyr. We compare purely irradiated cases with the irradiated plus extended heated ones. Even though the extra heat mostly inflates the outer layers, it leads to Ro increasing by about 1 order of magnitude in the inner layers, due to the higher internal entropy. Still, the dynamo region maintains $Ro < 0.1$, regardless of the stellar irradiation, so that we can infer that HJs remain in the fast-rotation regime. Since the evolutionary models depend on the irradiation alone, the results for Ro are the same for other stellar types, but shifted in orbital periods, as shown in App. A for MV3, KV3, and FV5 stars. HJs around the most massive star lead to larger inflation and higher values for Ro , but the dynamo region still remains lower than 0.1 in all cases. The sensitivity of results with planetary masses is discussed below.

In Fig. 6 we show the same upper right panel of Fig. 5 for the case with heat injection above the dynamo region. As expected from Fig. 4, there are large non-convective areas, where Ro is formally zero, in the metallic hydrogen region.

In Fig. 7 we show Ro for several different mass planets, for two representative orbital periods $P_{\text{orb}} = 2.45$ and 31.6 d, for both heated and non-heated models. We show four planetary masses, which well represent the monotonic trend with M_P . Heated and non-heated models are indistinguishable for long periods, as the $\epsilon(F_{\text{irr}})$ is negligible. As seen in the top panel of Fig. 7, inflation has minimal effect for planets above 8 M_J , with only a slight increase of Ro with a factor less than 2. Instead, a low-mass planet of 0.5 M_J experiences a more than one order of magnitude increase in Ro , although it remains in the fast rotator regime. This still has consequences for

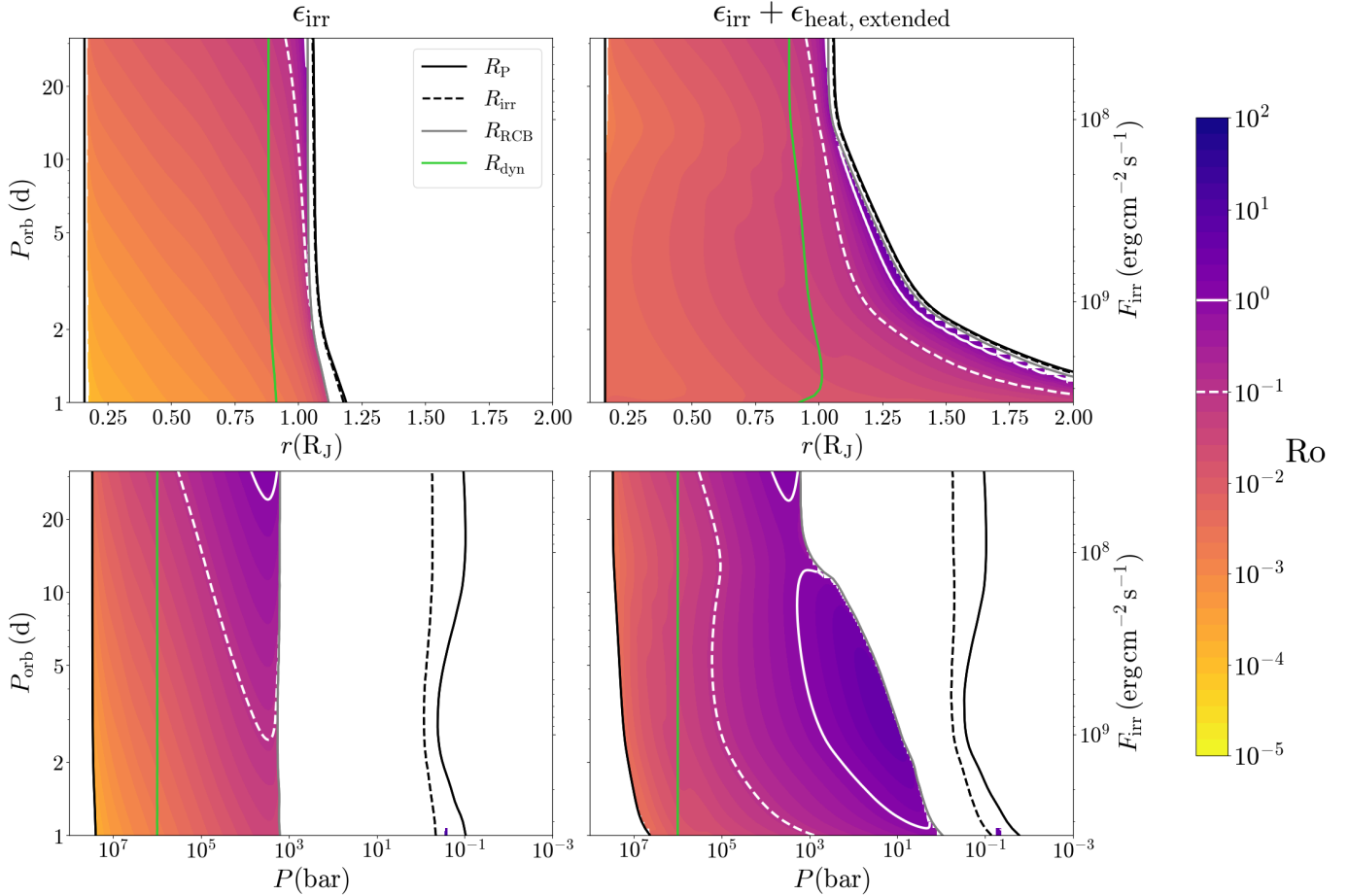


Figure 5. Rossby number as a function of radius or pressure for 1 M_J planets orbiting a solar-like G2 star, comparing heated (left panels) and non-heated (right panels) models. The different radii introduced in Fig. 2 are shown as in the legend, while the white lines mark $Ro=0.1$ (dashed) and $Ro=1$ (solid).

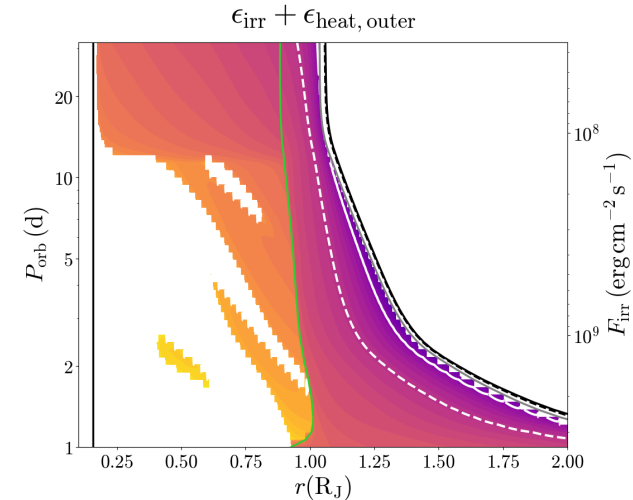


Figure 6. Similar to Fig. 5, but for the outer deposition of heat, i.e., only above the dynamo region.

the interior dynamics, as an increase in Ro may lead to more multipolar but weak dynamo-generated magnetic

fields (Christensen & Aubert 2006; Jones 2011; Davidson 2013).

Planets with longer P_{orb} but still tidally locked, as the ones shown on the top panel of Fig. 7, have the highest Ro . The most conductive layers of low-mass planets are generally well within the fast-rotation regime, but for masses higher than 4 M_J , a large fraction of their metallic hydrogen regions have $Ro \gtrsim 0.1$, being the only exceptions to the overall finding of this study. Note that for longer period planets, $P_{\text{orb}} > 15$ d, the heating mechanism is low and there is no inflation (see App. A). Therefore, the argument for convection suppression would not apply to high-mass long-period planets.

5. OBSERVATIONAL CONSEQUENCES

5.1. Magnetic field scaling laws

Combining energy equipartition arguments, the results for a large set of dynamo simulations (Christensen & Aubert 2006) and magnetic field measurements, Christensen et al. (2009) argued that for the

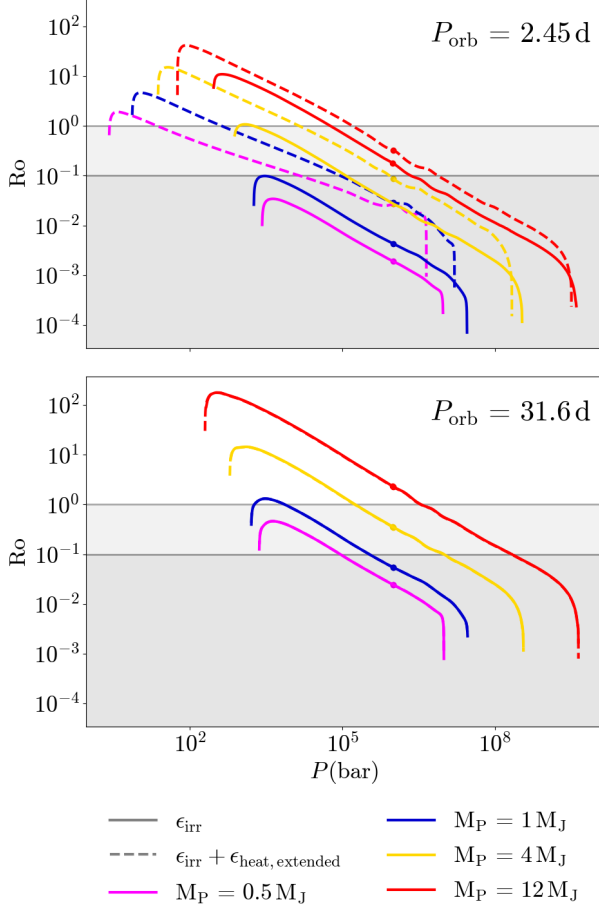


Figure 7. Rossby number as a function of pressure for different mass planets orbiting a G2 star with two different periods, comparing models with the extended heating (dashed) with only irradiated models (solid).

Earth, Jupiter, and fully-convective fast-rotating main-sequence stars, the convective heat flux is the key factor determining the order of magnitude of the dynamo-generated magnetic field strength:

$$\frac{B^2}{2\mu_0} \propto f_{\text{ohm}} \rho^{1/3} \left(\frac{q_c L}{H_T} \right)^{2/3}, \quad (13)$$

where μ_0 is the magnetic permeability, $f_{\text{ohm}} \leq 1$ is the ratio of ohmic to total dissipation, L is the length scale of the largest convective structures and $H_T = P/(\rho g \nabla_{\text{ad}})$ is the temperature scale height, with c_p the heat capacity, α the thermal expansion coefficient, g is the gravitational acceleration, and q_c is the convective heat flux as previously defined. As in Christensen et al. (2009), we hereafter assume $f_{\text{ohm}} = 1$ for simplicity. Eq. (13) can be integrated in the spherically symmetric shell of volume V (between R_{core} and R_{dyn}) and define the root-mean-square value of the magnetic field in the dynamo

region as:

$$\frac{B_{\text{dyn}}^2}{2\mu_0} := \frac{\langle B \rangle^2}{2\mu_0} = c f_{\text{ohm}} \langle \rho \rangle^{1/3} (F q_o)^{2/3}, \quad (14)$$

where brackets indicate volume averages, q_o is a reference convective flux, which we take as the value of q_c at R_{dyn} , c is a proportionality constant, calibrated as $c = 0.63$ by Christensen et al. (2009), and the factor F includes the radial profile variations as follows:

$$F^{2/3} = \frac{1}{V} \int_{R_{\text{core}}}^{R_{\text{dyn}}} \left(\frac{q_c(r)}{q_o} \frac{L(r)}{H_T(r)} \right)^{2/3} \left(\frac{\rho(r)}{\langle \rho \rangle} \right)^{1/3} 4\pi r^2 dr \quad (15)$$

where $L = \min(D, H_\rho)$. All these quantities are obtained for the evolutionary models at each timestep. This implementation is similar to other planetary studies (e.g. Hori 2021; Kilmetis et al. 2024).

Additionally, we can estimate the dipolar component at the planetary surface at the magnetic equator, $B_{\text{dip,surf}}$, defined as:

$$B_{\text{dip,surf}} = \frac{1}{2\sqrt{2}} \left(\frac{R_{\text{dyn}}}{R_P} \right)^3 B_{\text{dyn}}, \quad (16)$$

where for simplicity we use the same factor $1/(2\sqrt{2})$ as in Reiners & Christensen (2010), which comes from the assumption that the rms dipole field strength is half of the rms and that we consider the value at the magnetic equator, which is $1/\sqrt{2}$ of the average dipole field. Note also that the scaling law suffers of considerable uncertainties: (i) Reiners et al. (2009); Reiners & Christensen (2010) reformulate the original scaling law and evaluate a $\sim 60\%$ relative dispersion around that formula from data comparison; (ii) several factors (like the dipolar fraction and f_{ohm}) which may be in reality systematically shifted, or vary from case to case; (iii) the calibration of the scaling law has been originally limited to the Earth, Jupiter and low-mass main-sequence stars, excluding other planets, with brown dwarfs found later to be surprising outliers (Kao et al. 2016, 2018), and with no available comparison with magnetic field measurements for exoplanets, except a few indirect estimates by (Cauley et al. 2019). Therefore, the absolute values should be taken with care. Nevertheless, our main focus is to show the trends of the predicted field, mainly as a function of age, P_{orb} , and the type of heating.

Note also that, for each model, we show the evolution from 10 Myr to 10 Gyr. At early ages, convection is more vigorous, but more effects related to disk-planet interaction and migration could occur, which we do not account for. Moreover, as discussed above, the internal structure predicted by cooling models still depends on the specific initial entropy, while at later ages, $\gtrsim 0.1$

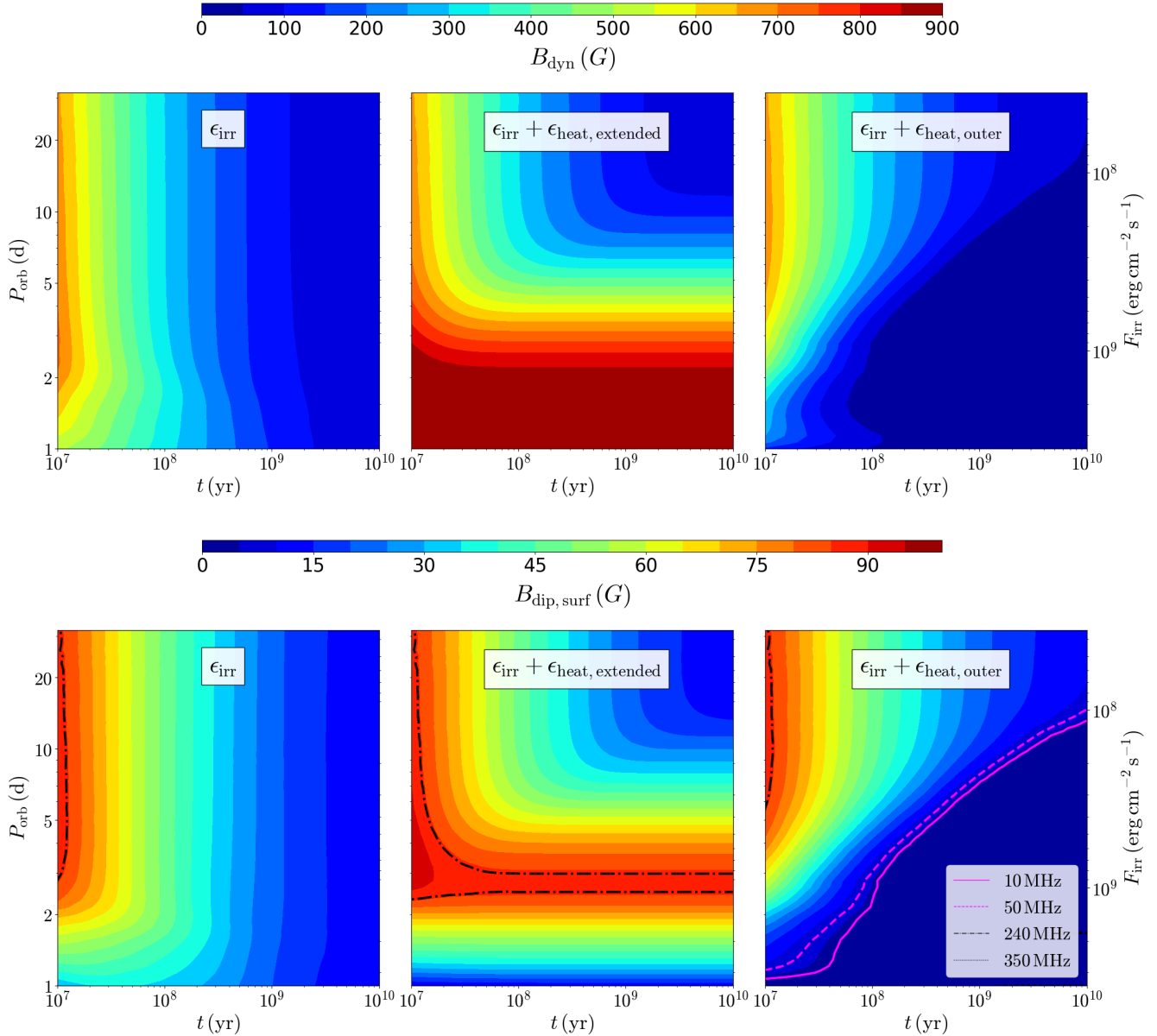


Figure 8. Magnetic field estimates for $1 M_J$ planets orbiting a $1 M_\odot$ main-sequence star (same models as Fig. 5 and 6). *Top panels:* average magnetic field strength at the dynamo surface obtained with the scaling law discussed in the text. *Bottom panels:* inferred dipole component at the planetary surface equator. Several of the most interesting frequency limits are included: 10 MHz, the ionospheric cut-off and lower range of LOFAR; 50 MHz, the lower range of SKA-low; 240 MHz, the upper range of LOFAR; and 350 MHz, the upper range of SKA-low.

Gyr, the evolution has lost memory of the initial condition, so that results are more reliable in this sense. Since the bulk of detected HJs are $\mathcal{O}(\text{Gyr})$ -old, hereafter we will not focus on the $t \lesssim 100$ Myr part of the plots.

In Fig. 8, we show B_{dyn} (top) and $B_{\text{dip,surf}}$ (bottom) for the same $1 M_J$ models shown in Fig. 5 and 6. Models with only irradiation (left panels) lead to a magnetic field decay in time ($B \propto t^{-0.3}$, where B can be $B_{\text{dip,surf}}$ or B_{dyn}) proportional to the gradual cooling of

the planet and independent of the orbital period, compatible with Reiners & Christensen (2010) and Elias-López et al. (2025). Models with internal heat lead instead to much higher $B_{\text{dip,surf}}$, since the shrinking is stalled, with an equilibrium between the long-term cooling and the internal heating. These values are compatible with Yadav & Thorngren (2017), which assumes that all the heat necessary to inflate the planet is involved with the magnetic field generation (see Viganò

et al. 2025 for a discussion about the assumptions in the use of the scaling laws). As seen in Fig. 2 and Fig. 3, inflation mostly affects the outer layers of the planet, and the dynamo region does not expand nearly as much. The consequence is that, even though B_{dyn} plateaus at very high values ~ 900 G for $P_{\text{orb}} \lesssim 2$ d, $B_{\text{dip,surf}}$ has much lower values, since the layers between the outer dynamo region R_{dyn} and the planetary surface R_{P} are inflated, and the relative decay of the dipolar field, cubic in radius, is relevant (higher multipoles decay even more). The non-heated models shown in Kilmetis et al. (2024) have a similar trend where the magnetic field estimation decays for short P_{orb} .

The predictions for models with the outer heating, for which convection can be suppressed, are very different, as shown in the right panels of Fig. 8. Whenever inflation becomes noticeable, the magnetic field strength dramatically decreases to values even lower than the Jovian values of ~ 10 G. The cases with the lowest predicted values of B_{dyn} have thin layers of convection below R_{dyn} . This implies that the integral, Eq. (15), is very sensitive to both the assumed definition of R_{dyn} , and the radial interval used in the outer heating. Moreover, it might not be accurate to estimate the magnetic field strength created in these shallower convective layers with the same scaling laws. Therefore, the values shown on the left panel of Fig. 8 could be even lower or potentially vanish for the convection-suppressed cases.

This fact leads us to draw a parallel with Venus. The most accepted argument for the lack of an active Venusian dynamo is the presence of a stagnant lid. The absence of an active tectonic plate system hinders the efficient cooling of its core, resulting in steeper entropy gradients (Nimmo 2002; Jacobson et al. 2017). The argument works similarly for HJs: if the heating necessary to reach the observed HJ radii is deposited in the outer layers, convection (and thus dynamo) is suppressed, essentially due to a blanketing effect.

5.2. Planetary coherent radio emission

One of the main observational consequences of exoplanetary magnetic fields is the possible coherent radio emission, as seen in all magnetized planets in the Solar system (Zarka 1998). The mechanism behind this emission is the above-mentioned ECM (Dulk 1985), which requires the presence of a source of keV electrons (arguably coming from the stellar wind) and a planetary magnetic field. As the charged particles from the stellar wind come into the vicinity of the planetary magnetic field, they start following helical trajectories around the magnetic field lines and get bunched together in phase. This results in a coherent, circularly polarized radio

emission from the planet in a hollow cone, at the Larmor frequency of the local magnetic field B , ν_c [MHz] = $2.8B$ [G]. Therefore, the detected emission traces the intensity of the magnetic field, with a frequency cut-off at the Larmor frequency of the largest value of the field in the emitting region, i.e., close to the surface. As seen in the bottom panel of Fig. 8, irradiated and extended heated models have $B_{\text{dip,surf}}$ estimations that surpass the ~ 10 MHz ionospheric cut-off, which corresponds to a minimum magnetic field strength of ~ 3.5 G. On the contrary, when HJ are inflated with the outer heating, their $B_{\text{dip,surf}}$ usually are below the ECM cut-off, suppressing any detectable radio emission.

Given that the Jovian case remains the only firm observable constraint for gas giants' ECM emission, there are huge uncertainties on how bright the expected radio emission should be. Simple estimates assume that the emitted radio power is proportional to the kinetic flux intercepted by the planetary magnetosphere and is given by the phenomenological radiometric Bode's law, which fits the well-characterized radio luminosity of Jupiter and the one from the other solar planets, which are less studied, coming mostly from limited in-situ Cassini and Voyager measurements. The corresponding specific flux, scaled by the measured typical Jovian values, reads (Bastian et al. 2000; Zarka et al. 2001; Stevens 2005):

$$F_r = 2.35 \cdot 10^{-2} \text{ mJy} \cdot \left(\frac{\dot{M}_\star}{\dot{M}_\odot} \right)^{2/3} \cdot \left(\frac{M_{\text{dip}}}{M_{\text{dip,J}}} \right)^{2/3} \cdot \left(\frac{a}{5 \text{ AU}} \right)^{-4/3} \cdot \left(\frac{V_W}{400 \text{ km s}^{-1}} \right)^{5/3} \cdot \left(\frac{d}{10 \text{ pc}} \right)^{-2} \quad (17)$$

where \dot{M}_\star is the stellar mass loss rate, $M_{\text{dip}} = B_{\text{dip,surf}} R_{\text{P}}^3$ is the planetary magnetic dipolar moment, and d is the distance to the source. The stellar wind properties may vary from case to case and can be inferred from UV and X-ray observations (see e.g. (Wood et al. 2021) for M dwarfs), or some models (e.g., Johnstone et al. 2015). Given the intrinsic uncertainties, here we simply assume a representative solar value, $\dot{M}_\star = \dot{M}_\odot \simeq 400 \text{ km s}^{-1}$ (Wood et al. 2005), thus neglecting the large spatial and time variability measured for the Sun (e.g., Fig. 1 of Johnstone et al. 2015), and its dependence on a from measurements or from e.g. the Parker (1965) model.

In the top panel of Fig. 9, we show the resulting estimates for the ECM radio flux, for the same models in Fig. 8. HJs with extended heating have very high flux predictions, overcoming 1 Jy, which is incompatible with much lower upper limits reported in literature for tens of HJs (e.g. Narang et al. 2024 and references within). Models with external heating have instead flux

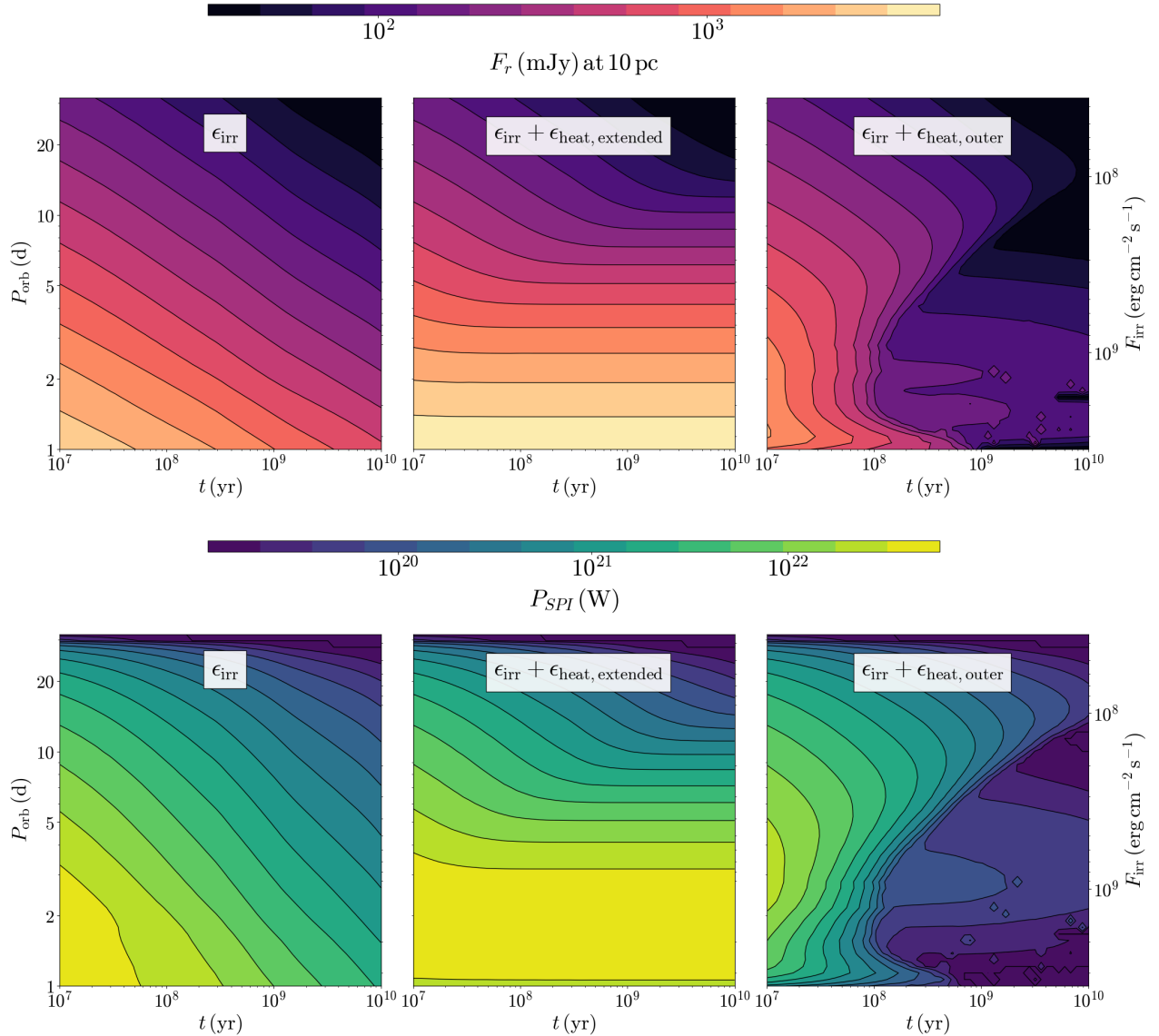


Figure 9. Estimates for Jovian-like coherent radio flux (top, for a 10 pc away HJ) and SPI available power (bottom), as a function of age and P_{orb} , for the same models shown in Fig. 8.

estimates which are orders of magnitude smaller, especially for the hottest cases at Gyr ages, where the convection and dynamo suppression bring the most relevant effects. Moreover, they are mostly below the 10 MHz ionospheric cut-off shown in Fig. 8 and cannot be detected by ground-based radio interferometers.

Note that the absolute values of the estimated flux for the purely irradiated case are compatible with the cases proposed in the original works by e.g. Stevens (2005), and fluxes $F_r \gtrsim 0.1$ mJy should be easily detectable by targeted observations and/or current wide-field radio surveys at low frequencies, LOFAR Stokes V survey V-LoTSS in particular (Callingham et al. 2023). However, after two decades of radio campaigns targeting tens of

theoretically promising HJs have led to no confirmed planetary radio emission (see e.g. Fig. 6 of Narang et al. 2024, and references within), with a claim for one case (Turner et al. 2021), not confirmed by an extended follow-up (Turner et al. 2024). Therefore, the models are probably very optimistic, in part because they are often calibrated to the peak values of the Jovian short bursts, rather than the average one. In any case, the purpose of this work is to discuss the trends with irradiation and heating models, rather than the absolute values, which are arguably plagued by huge intrinsic uncertainties.

5.3. Star-planet interaction available power

Another potentially observable signature of planetary magnetism is the effect of magnetic SPI. One of the possible SPI mechanisms for HJ systems can arise when a close-in giant planet moves through its host star’s magnetic field, enabling energy transfer due to the stretching of magnetic flux tubes that connect the planetary and stellar magnetospheres (Lanza 2013). This interaction can produce observable signatures, such as spectroscopically detectable modulation with the orbital period of chromospheric activity (in particular, the emission line Ca II K, Cauley et al. 2019), or coherent emission at radio frequencies close to the stellar surface (e.g., Saur et al. 2013; Pérez-Torres et al. 2021). Here we don’t enter into detail of the specific manifestation of the SPI at different wavelengths, but we simply follow Lanza (2013) to derive the total power available:

$$P_{\text{SPI}} \simeq \frac{2\pi}{\mu_o} f_{\text{AP}} R_{\text{P}}^2 (2B_{\text{dip,surf}})^2 v_{\text{rel}}, \quad (18)$$

where $v_{\text{rel}} = 2\pi a/P_{\text{rel}}$ is the relative velocity between the planet and the stellar magnetic field lines (therefore, $P_{\text{rel}} = 2\pi/(\omega_{\text{orb}} - \omega_{\star})$, where ω_i are orbital frequencies), $2B_{\text{dip,surf}}$ is the polar magnetic field (twice its equatorial value defined in Eq. 16), and f_{AP} is the fraction of the planetary surface covered by stellar magnetic flux tubes:

$$f_{\text{AP}} = 1 - \left(1 - \frac{3\xi^{1/3}}{2 + \xi}\right)$$

where $\xi = B_{\star}(a)/(2B_{\text{dip,surf}})$. $B_{\star}(a)$ is the stellar magnetic field at the given orbital separation, which we derive assuming a solar-like value at the stellar surface for simplicity, $B_{\star} = 10$ G. Note that this underestimates the stellar field for at least M dwarfs, which, being fully convective, usually show hundreds to thousands gauss fields (Reiners et al. 2022), and for the highly magnetic, chemically peculiar Ap and Bp stars. However, the bulk of HJs orbit Sun-like stars whose spectral type is usually associated with (at most) Sun-like large-scale magnetic field values (e.g., Seach et al. 2020), therefore justifying our simple assumption.

Eq. (18) estimates the Poynting flux generated by the continuous stretching of magnetic field lines due to the planet’s motion and was also used in Cauley et al. (2019) to estimate the magnetic field of four HJs by observing periodic enhancements in the Ca II K chromospheric emission line. In the same work, they show that other SPI estimates, like the pioneering reconnection model (Cuntz et al. 2000) and the Alfvén wing scenario (Saur et al. 2013; Strugarek 2016), have different dependencies with the planetary and stellar magnetic fields, and typically provide less available power, incompatible with

the observed activity modulation signal (Cauley et al. 2019), so we don’t discuss them here. In the bottom panels of Fig. 9, we show the resulting available SPI power, a fraction of which (e.g., $\lesssim 1\%$ in Cauley et al. 2019) can become visible as orbit-modulation of the activity indicators. Similar to Fig. 8, only the extended heat scenario, for the hottest cases, provide optimistic predictions for inflated HJs, $P_{\text{SPI}} \gtrsim 10^{22}$ W, potentially able then to power the observationally inferred values of 10^{20} W in Ca II K line modulation, assuming reasonable $\lesssim 1\%$ conversion efficiency, Cauley et al. 2019. When the heat is applied only above the dynamo, the available power is typically reduced by orders of magnitude.

Note that an essential requirement for SPI is that the local wind velocity should be less than the Alfvén velocity (i.e., the Alfvén Mach number $M_A = v_W/v_{\text{alf}} < 1$, where v_{alf} is the Alfvén speed). This intrinsically depends on the individual stellar properties, and we cannot assess it here. However, it can further limit the detectability of SPI signals. Therefore, again, the values here indicated should be regarded as upper limits and be used to only infer the trends with the HJ properties (depending ultimately on irradiation and heating).

6. CONCLUSIONS

In this work, we model the interior evolutionary tracks of inflated hot Jupiters using the one-dimensional evolutionary code MESA. We assume tidal locking and irradiation from main-sequence host stars, and we explore dependencies on orbital distance, planetary and stellar mass, and the type of heat injection. Guided by observationally constrained flux-heating efficiency relations (Thorngren & Fortney 2018), we inject heat into the internal layers of the planet to reproduce the observed radii. This relation and others in the literature (e.g. Sarkis et al. (2021)) have big dispersions around average values of inflated radii, for a given irradiation. Therefore, this study only addresses the trends with the planetary properties (mass, separation, type of internal heating), keeping the parameters involving the amount of deposited heat fixed.

For a given stellar type, orbital period and planetary mass, we compare the purely irradiated case with two simplified scenarios of regions where extra heat is continuously deposited: extended (injected mostly in the dynamo region, $P \gtrsim 10^6$ bar), or outside the dynamo region, which is what is expected in most models, the Ohmic one especially (Batygin & Stevenson 2010; Batygin et al. 2011; Thorngren 2024; Viganò et al. 2025). Whether heat is injected uniformly, centrally, or throughout the convective region, the structural differences are minimal. Planets typically exhibit a shallow

stratified outer layer, which fully contains the irradiation zone, followed by a deep convective interior where pressure is sufficient for hydrogen metallization and possible dynamo action.

However, important differences are seen in the Rossby number as a function of depth. The vast majority of models yield $Ro \lesssim 0.1$, indicating a fast-rotating convection regime. Defining HJs as having $P_{orb} < 10$ d or $T_{eq} > 1000$ K (see Gan et al. (2023) and within), we can safely say that the vast majority of confirmed HJs are expected to be in the low- Ro regime. Only the most massive, distantly orbiting (yet still tidally locked) planets exceed $Ro \gtrsim 0.1$ over significant interior regions, potentially altering the dynamo regime. Thus, massive HJs with orbital periods beyond 15-20 days may host low-Rossby-number dynamos that generate weaker, more multipolar magnetic fields despite similar convective power. Within the known HJs, only three targets with $M_P \gtrsim 4 M_J$ closer than 100 pc have $15 \text{ d} < P_{orb} < 40 \text{ d}$, all orbiting G-type stars. The most promising candidate to test their potential peculiarity is GJ 86 b (Stassun et al. 2017), which has a 15.8 d orbit, a mass of $4.4 M_J$, and is located only at 10.8 pc. The other two planets are farther away: HD 72892 b (39.4 d, $5.5 M_J$, 69.7 pc, Feng et al. (2022)) and TIC 393818343 b (16.2 d, $4.3 M_J$, 93.7 pc, Sgro et al. (2024)).

The extra heat affects the outer layers and consistently increases Ro . While this effect is negligible for planets above $8 M_J$ (especially those already exceeding $Ro \gtrsim 0.1$), which can hardly get inflated due to their higher gravity, lower-mass planets experience a roughly one order of magnitude increase in Ro , which has important interior dynamic consequences even if they remain within the low- Ro regime. When the heat injection is localized outside the dynamo region, the temperature gradients are reduced or even inverted, as already briefly mentioned by e.g. (Komacek & Youdin 2017; Komacek et al. 2020). The internal heat transport is significantly reduced, leading to positive entropy gradients that suppress convection.

The relevant consequence of this comes when one applies the widely-used, observationally constrained magnetic scaling laws from Christensen et al. (2009), suited for fast rotators. When heat is deposited in an extended way, we recover surface magnetic field strengths around 100 G for the most inflated planets, an order of magnitude higher than Jupiter. These estimates are compatible with the work of Yadav & Thorngren (2017), who assume that the convective heat flux is given by the extra heat. This is conceptually similar to our extended heat case, where heat is essentially deposited in the dynamo region. In contrast, a more realistic exter-

nal heating substantially reduces convective power and yields weaker magnetic fields.

This result is particularly interesting in the context of the Ohmic dissipation models (Batygin & Stevenson 2010; Batygin et al. 2011; Perna et al. 2010a; Wu & Lithwick 2013; Ginzburg & Sari 2016; Knierim et al. 2022; Viganò et al. 2025). Essentially, it relies on the presence of conducting outermost layers due to thermal ionization (e.g., Kumar et al. 2021; Dietrich et al. 2022), and on the circulation of strong, mainly zonal winds which twist and stretch the background field coming from the deep-seated dynamo. The induced currents propagate and dissipate into the interior as well, due to the finite values of conductivity in the outer convective region (much smaller than in the dynamo region, but not zero). Combining estimation for the conductivity and the induced currents, models predict that the Ohmic heating profile steeply decays towards the interior, so that the bulk of it is deposited well above the dynamo region (Batygin et al. 2011; Ginzburg & Sari 2016; Knierim et al. 2022; Viganò et al. 2025). Since the atmospheric induction depends also on the intensity of the background magnetic field (in a linear way only for magnetic Reynolds numbers $Rm \lesssim 1$), there could be an interesting, non-trivial coupling between the dynamo and the atmospheric induction: if the Ohmic heating is large, it can suppress convection and the underlying dynamo field, which would in turn decrease the Ohmic heating rate, causing the convection to be restored. This process might only lead to a less effective Ohmic heating mechanism or, potentially, show an oscillatory behavior, as proposed by Viganò et al. (2025).

The considerations on the magnetic field strengths are of direct interest for the observational detection of SPI signals (Cauley et al. 2019), and/or planetary Jovian-like coherent radio emission, which remains elusive, despite optimistic predictions (Stevens 2005) and tens of observational campaigns (e.g., Narang et al. 2024 and references within). Several potential causes can account for the lack of detection, including the beaming effect, large distances, intrinsic variability, and limited observational coverage. However, one cannot neglect the possibility that the typical estimates of HJ magnetic fields of the order 100 G might be too optimistic (Yadav & Thorngren 2017; Kilmatis et al. 2024). In this sense, our results indicate that very massive HJs might offer an exception, since their internal structure is less sensitive to the combined effects of irradiation and heating, and could maintain large magnetic fields. For Jupiter-like masses, if the external heating model is assumed, there is little hope of having a magnetic field much larger than Jupiter.

ACKNOWLEDGEMENTS

AEL, SK and CSG's work has been carried out within the framework of the doctoral program in Physics of the Universitat Autònoma de Barcelona. AEL, DV, SK and CSG are supported by the European Research Council (ERC) under the European Union's Horizon 2020 research and innovation program (ERC Starting Grant "IMAGINE" No. 948582, PI: DV) and the support from the "María de Maeztu" award to the Institut de Ciències de l'Espai (CEX2020-001058-M). AEL gratefully acknowledges the support and hospitality from the Simons Foundation through the predoctoral program at

the Center for Computational Astrophysics, Flatiron Institute. The computational resources and services used in this work were provided by facilities supported by the Scientific Computing Core at the Flatiron Institute, a division of the Simons Foundation. We also acknowledge using the MareNostrum BSC supercomputer of the Spanish Supercomputing Network via project RES/BSC Call AECT-2024-2-0011 (PI AEL). FDS acknowledges support from a Marie Curie Action of the European Union (Grant agreement 101030103). This research has made use of the NASA Exoplanet Archive, which is operated by the California Institute of Technology, under contract with the National Aeronautics and Space Administration under the Exoplanet Exploration Program.

REFERENCES

- Arras, P., & Bildsten, L. 2006, *ApJ*, 650, 394, doi: [10.1086/506011](https://doi.org/10.1086/506011)
- Bastian, T. S., Dulk, G. A., & Leblanc, Y. 2000, *ApJ*, 545, 1058, doi: [10.1086/317864](https://doi.org/10.1086/317864)
- Batygin, K. 2018, *AJ*, 155, 178, doi: [10.3847/1538-3881/aab54e](https://doi.org/10.3847/1538-3881/aab54e)
- Batygin, K., & Stevenson, D. J. 2010, *The Astrophysical Journal Letters*, 714, L238, doi: [10.1088/2041-8205/714/2/L238](https://doi.org/10.1088/2041-8205/714/2/L238)
- Batygin, K., Stevenson, D. J., & Bodenheimer, P. H. 2011, *ApJ*, 738, 1, doi: [10.1088/0004-637X/738/1/1](https://doi.org/10.1088/0004-637X/738/1/1)
- Bonitz, M., Vorberger, J., Bethkenhagen, M., et al. 2024, *Physics of Plasmas*, 31, 110501, doi: [10.1063/5.0219405](https://doi.org/10.1063/5.0219405)
- Burrows, A., Hubeny, I., Budaj, J., & Hubbard, W. B. 2007, *ApJ*, 661, 502, doi: [10.1086/514326](https://doi.org/10.1086/514326)
- Callingham, J. R., Shimwell, T. W., Vedantham, H. K., et al. 2023, *A&A*, 670, A124, doi: [10.1051/0004-6361/202245567](https://doi.org/10.1051/0004-6361/202245567)
- Carroll, B. W., & Ostlie, D. A. 2017, *An introduction to modern astrophysics*, Second Edition
- Cauley, P. W., Shkolnik, E. L., Llama, J., & Lanza, A. F. 2019, *Nature Astronomy*, 3, 1128, doi: [10.1038/s41550-019-0840-x](https://doi.org/10.1038/s41550-019-0840-x)
- Chabrier, G., & Baraffe, I. 2007, *ApJL*, 661, L81, doi: [10.1086/518473](https://doi.org/10.1086/518473)
- Christensen, U. R., & Aubert, J. 2006, *Geophysical Journal International*, 166, 97, doi: [10.1111/j.1365-246X.2006.03009.x](https://doi.org/10.1111/j.1365-246X.2006.03009.x)
- Christensen, U. R., Holzwarth, V., & Reiners, A. 2009, *Nature*, 457, 167, doi: [10.1038/nature07626](https://doi.org/10.1038/nature07626)
- Christiansen, J. L., McElroy, D. L., Harbut, M., et al. 2025, *arXiv e-prints*, arXiv:2506.03299, doi: [10.48550/arXiv.2506.03299](https://doi.org/10.48550/arXiv.2506.03299)
- Cox, J. P., & Giuli, R. T. 1968, *Principles of stellar structure*
- Cuntz, M., Saar, S. H., & Musielak, Z. E. 2000, *ApJL*, 533, L151, doi: [10.1086/312609](https://doi.org/10.1086/312609)
- Dang, L., Cowan, N. B., Schwartz, J. C., et al. 2018, *Nature Astronomy*, 2, 220, doi: [10.1038/s41550-017-0351-6](https://doi.org/10.1038/s41550-017-0351-6)
- Davidson, P. A. 2013, *Geophysical Journal International*, 195, 67, doi: [10.1093/gji/ggt167](https://doi.org/10.1093/gji/ggt167)
- de Gasperin, F., Brunetti, G., Bruggen, M., et al. 2020, doi: [10.26093/cds/vizier.36420085](https://doi.org/10.26093/cds/vizier.36420085)
- Dietrich, W., Kumar, S., Poser, A. J., et al. 2022, *MNRAS*, 517, 3113, doi: [10.1093/mnras/stac2849](https://doi.org/10.1093/mnras/stac2849)
- Dulk, G. A. 1985, *ARA&A*, 23, 169, doi: [10.1146/annurev.aa.23.090185.001125](https://doi.org/10.1146/annurev.aa.23.090185.001125)
- Elias-López, A., Del Sordo, F., Viganò, D., et al. 2025, *A&A*, 696, A161, doi: [10.1051/0004-6361/202453372](https://doi.org/10.1051/0004-6361/202453372)
- Feng, F., Butler, R. P., Vogt, S. S., et al. 2022, *ApJS*, 262, 21, doi: [10.3847/1538-4365/ac7e57](https://doi.org/10.3847/1538-4365/ac7e57)
- Fortney, J. J., Dawson, R. I., & Komacek, T. D. 2021, *Journal of Geophysical Research (Planets)*, 126, e06629, doi: [10.1029/2020JE006629](https://doi.org/10.1029/2020JE006629)
- Fortney, J. J., Marley, M. S., & Barnes, J. W. 2007, *ApJ*, 659, 1661, doi: [10.1086/512120](https://doi.org/10.1086/512120)
- French, M., Becker, A., Lorenzen, W., et al. 2012, *The Astrophysical Journal Supplement Series*, 202, 5, doi: [10.1088/0067-0049/202/1/5](https://doi.org/10.1088/0067-0049/202/1/5)
- Fuentes, R., Cumming, A., Anders, E., & Hindman, B. 2023, in *AAS/Division for Planetary Sciences Meeting Abstracts*, Vol. 55, AAS/Division for Planetary Sciences Meeting Abstracts #55, 302.06
- Gan, T., Wang, S. X., Wang, S., et al. 2023, *AJ*, 165, 17, doi: [10.3847/1538-3881/ac9b12](https://doi.org/10.3847/1538-3881/ac9b12)
- Ginzburg, S., & Sari, R. 2015, *ApJ*, 803, 111, doi: [10.1088/0004-637X/803/2/111](https://doi.org/10.1088/0004-637X/803/2/111)

- . 2016, *ApJ*, 819, 116, doi: [10.3847/0004-637X/819/2/116](https://doi.org/10.3847/0004-637X/819/2/116)
- Goldreich, P., & Soter, S. 1966, *Icarus*, 5, 375, doi: [10.1016/0019-1035\(66\)90051-0](https://doi.org/10.1016/0019-1035(66)90051-0)
- Grieffmeier, J. M., Zarka, P., & Spreeuw, H. 2007, *A&A*, 475, 359, doi: [10.1051/0004-6361:20077397](https://doi.org/10.1051/0004-6361:20077397)
- Guillot, T., Burrows, A., Hubbard, W. B., Lunine, J. I., & Saumon, D. 1996, *ApJL*, 459, L35, doi: [10.1086/309935](https://doi.org/10.1086/309935)
- Guillot, T., & Showman, A. P. 2002, *A&A*, 385, 156, doi: [10.1051/0004-6361:20011624](https://doi.org/10.1051/0004-6361:20011624)
- Heng, K., & Showman, A. P. 2015, *Annual Review of Earth and Planetary Sciences*, 43, 509, doi: [10.1146/annurev-earth-060614-105146](https://doi.org/10.1146/annurev-earth-060614-105146)
- Hori, Y. 2021, *ApJ*, 908, 77, doi: [10.3847/1538-4357/abd8d1](https://doi.org/10.3847/1538-4357/abd8d1)
- Jacobson, S. A., Rubie, D. C., Hernlund, J., Morbidelli, A., & Nakajima, M. 2017, *Earth and Planetary Science Letters*, 474, 375, doi: [10.1016/j.epsl.2017.06.023](https://doi.org/10.1016/j.epsl.2017.06.023)
- Jermyn, A. S., & Cantiello, M. 2020, *ApJ*, 900, 113, doi: [10.3847/1538-4357/ab9e70](https://doi.org/10.3847/1538-4357/ab9e70)
- Jermyn, A. S., Bauer, E. B., Schwab, J., et al. 2023, *ApJS*, 265, 15, doi: [10.3847/1538-4365/aca8e8](https://doi.org/10.3847/1538-4365/aca8e8)
- Johnstone, C. P., Güdel, M., Lüftinger, T., Toth, G., & Brott, I. 2015, *A&A*, 577, A27, doi: [10.1051/0004-6361/201425300](https://doi.org/10.1051/0004-6361/201425300)
- Jones, C. A. 2011, *Annual Review of Fluid Mechanics*, 43, 583, doi: [10.1146/annurev-fluid-122109-160727](https://doi.org/10.1146/annurev-fluid-122109-160727)
- Kao, M. M., Hallinan, G., Pineda, J. S., et al. 2016, *ApJ*, 818, 24, doi: [10.3847/0004-637X/818/1/24](https://doi.org/10.3847/0004-637X/818/1/24)
- Kao, M. M., Hallinan, G., Pineda, J. S., Stevenson, D., & Burgasser, A. 2018, *ApJS*, 237, 25, doi: [10.3847/1538-4365/aac2d5](https://doi.org/10.3847/1538-4365/aac2d5)
- Kilmetis, K., Vidotto, A. A., Allan, A., & Kubyskhina, D. 2024, *MNRAS*, 535, 3646, doi: [10.1093/mnras/stae2505](https://doi.org/10.1093/mnras/stae2505)
- Knierim, H., Batygin, K., & Bitsch, B. 2022, *A&A*, 658, L7, doi: [10.1051/0004-6361/202142588](https://doi.org/10.1051/0004-6361/202142588)
- Knutson, H. A., Charbonneau, D., Allen, L. E., et al. 2007, *Nature*, 447, 183, doi: [10.1038/nature05782](https://doi.org/10.1038/nature05782)
- Komacek, T. D., Thorngren, D. P., Lopez, E. D., & Ginzburg, S. 2020, *ApJ*, 893, 36, doi: [10.3847/1538-4357/ab7eb4](https://doi.org/10.3847/1538-4357/ab7eb4)
- Komacek, T. D., & Youdin, A. N. 2017, *ApJ*, 844, 94, doi: [10.3847/1538-4357/aa7b75](https://doi.org/10.3847/1538-4357/aa7b75)
- Kuhfuss, R. 1986, *A&A*, 160, 116
- Kumar, S., Poser, A. J., Schöttler, M., et al. 2021, *PhRvE*, 103, 063203, doi: [10.1103/PhysRevE.103.063203](https://doi.org/10.1103/PhysRevE.103.063203)
- Lanza, A. F. 2013, *A&A*, 557, A31, doi: [10.1051/0004-6361/201321790](https://doi.org/10.1051/0004-6361/201321790)
- Laughlin, G., Crismani, M., & Adams, F. C. 2011, *ApJL*, 729, L7, doi: [10.1088/2041-8205/729/1/L7](https://doi.org/10.1088/2041-8205/729/1/L7)
- Lazovik, Y. A. 2023, *MNRAS*, 520, 3749, doi: [10.1093/mnras/stad394](https://doi.org/10.1093/mnras/stad394)
- Li, J., & Goodman, J. 2010, *ApJ*, 725, 1146, doi: [10.1088/0004-637X/725/1/1146](https://doi.org/10.1088/0004-637X/725/1/1146)
- Lopez, E. D., & Fortney, J. J. 2016, *ApJ*, 818, 4, doi: [10.3847/0004-637X/818/1/4](https://doi.org/10.3847/0004-637X/818/1/4)
- Menou, K. 2012, *ApJ*, 745, 138, doi: [10.1088/0004-637X/745/2/138](https://doi.org/10.1088/0004-637X/745/2/138)
- Murray, C. D., & Dermott, S. F. 1999, doi: [10.1017/CBO9781139174817](https://doi.org/10.1017/CBO9781139174817)
- Narang, M., Puravankara, M., Ishwara Chandra, C. H., et al. 2024, *MNRAS*, 529, 1161, doi: [10.1093/mnras/stae536](https://doi.org/10.1093/mnras/stae536)
- Nimmo, F. 2002, *Geology*, 30, 987, doi: [10.1130/0091-7613\(2002\)030<0987:WDVLAM>2.0.CO;2](https://doi.org/10.1130/0091-7613(2002)030<0987:WDVLAM>2.0.CO;2)
- Parker, E. N. 1965, *SSRv*, 4, 666, doi: [10.1007/BF00216273](https://doi.org/10.1007/BF00216273)
- Paxton, B., Bildsten, L., Dotter, A., et al. 2011, *ApJS*, 192, 3, doi: [10.1088/0067-0049/192/1/3](https://doi.org/10.1088/0067-0049/192/1/3)
- Paxton, B., Cantiello, M., Arras, P., et al. 2013, *ApJS*, 208, 4, doi: [10.1088/0067-0049/208/1/4](https://doi.org/10.1088/0067-0049/208/1/4)
- Paxton, B., Marchant, P., Schwab, J., et al. 2015, *ApJS*, 220, 15, doi: [10.1088/0067-0049/220/1/15](https://doi.org/10.1088/0067-0049/220/1/15)
- Paxton, B., Schwab, J., Bauer, E. B., et al. 2018, *ApJS*, 234, 34, doi: [10.3847/1538-4365/aaa5a8](https://doi.org/10.3847/1538-4365/aaa5a8)
- Paxton, B., Smolec, R., Schwab, J., et al. 2019, *ApJS*, 243, 10, doi: [10.3847/1538-4365/ab2241](https://doi.org/10.3847/1538-4365/ab2241)
- Pérez-Torres, M., Gómez, J. F., Ortiz, J. L., et al. 2021, *A&A*, 645, A77, doi: [10.1051/0004-6361/202039052](https://doi.org/10.1051/0004-6361/202039052)
- Perna, R., Menou, K., & Rauscher, E. 2010a, *ApJ*, 724, 313, doi: [10.1088/0004-637X/724/1/313](https://doi.org/10.1088/0004-637X/724/1/313)
- . 2010b, *ApJ*, 719, 1421, doi: [10.1088/0004-637X/719/2/1421](https://doi.org/10.1088/0004-637X/719/2/1421)
- Reiners, A., Basri, G., & Christensen, U. R. 2009, *ApJ*, 697, 373, doi: [10.1088/0004-637X/697/1/373](https://doi.org/10.1088/0004-637X/697/1/373)
- Reiners, A., & Christensen, U. R. 2010, *A&A*, 522, A13, doi: [10.1051/0004-6361/201014251](https://doi.org/10.1051/0004-6361/201014251)
- Reiners, A., Schüssler, M., & Passetger, V. M. 2014, *ApJ*, 794, 144, doi: [10.1088/0004-637X/794/2/144](https://doi.org/10.1088/0004-637X/794/2/144)
- Reiners, A., Shulyak, D., Käpylä, P. J., et al. 2022, *A&A*, 662, A41, doi: [10.1051/0004-6361/202243251](https://doi.org/10.1051/0004-6361/202243251)
- Sánchez-Lavega, A. 2004, *ApJL*, 609, L87, doi: [10.1086/422840](https://doi.org/10.1086/422840)
- Sarkis, P., Mordasini, C., Henning, T., Marleau, G. D., & Mollière, P. 2021, *A&A*, 645, A79, doi: [10.1051/0004-6361/202038361](https://doi.org/10.1051/0004-6361/202038361)
- Saumon, D., Chabrier, G., & van Horn, H. M. 1995, *ApJS*, 99, 713, doi: [10.1086/192204](https://doi.org/10.1086/192204)
- Saur, J., Grambusch, T., Duling, S., Neubauer, F. M., & Simon, S. 2013, *A&A*, 552, A119, doi: [10.1051/0004-6361/201118179](https://doi.org/10.1051/0004-6361/201118179)
- Scharf, C. A. 2010, *ApJ*, 722, 1547, doi: [10.1088/0004-637X/722/2/1547](https://doi.org/10.1088/0004-637X/722/2/1547)

- Seach, J. M., Marsden, S. C., Carter, B. D., et al. 2020, MNRAS, 494, 5682, doi: [10.1093/mnras/staa1107](https://doi.org/10.1093/mnras/staa1107)
- Sestovic, M., Demory, B.-O., & Queloz, D. 2018, A&A, 616, A76, doi: [10.1051/0004-6361/201731454](https://doi.org/10.1051/0004-6361/201731454)
- Sgro, L. A., Dalba, P. A., Esposito, T. M., et al. 2024, AJ, 168, 26, doi: [10.3847/1538-3881/ad5096](https://doi.org/10.3847/1538-3881/ad5096)
- Showman, A. P., Fortney, J. J., Lian, Y., et al. 2009, ApJ, 699, 564, doi: [10.1088/0004-637X/699/1/564](https://doi.org/10.1088/0004-637X/699/1/564)
- Showman, A. P., & Guillot, T. 2002, A&A, 385, 166, doi: [10.1051/0004-6361:20020101](https://doi.org/10.1051/0004-6361:20020101)
- Soriano-Guerrero, C., Viganò, D., Perna, R., Akgün, T., & Palenzuela, C. 2023, MNRAS, 525, 626, doi: [10.1093/mnras/stad2311](https://doi.org/10.1093/mnras/stad2311)
- Soriano-Guerrero, C., Viganò, D., Perna, R., Elias-López, A., & Beltz, H. 2025, arXiv e-prints, arXiv:2505.14342, doi: [10.48550/arXiv.2505.14342](https://doi.org/10.48550/arXiv.2505.14342)
- Spiegel, D. S., & Burrows, A. 2013, ApJ, 772, 76, doi: [10.1088/0004-637X/772/1/76](https://doi.org/10.1088/0004-637X/772/1/76)
- Stassun, K. G., Collins, K. A., & Gaudi, B. S. 2017, AJ, 153, 136, doi: [10.3847/1538-3881/aa5df3](https://doi.org/10.3847/1538-3881/aa5df3)
- Stevens, I. R. 2005, MNRAS, 356, 1053, doi: [10.1111/j.1365-2966.2004.08528.x](https://doi.org/10.1111/j.1365-2966.2004.08528.x)
- Strugarek, A. 2016, ApJ, 833, 140, doi: [10.3847/1538-4357/833/2/140](https://doi.org/10.3847/1538-4357/833/2/140)
- Thorngren, D. P. 2024, arXiv e-prints, arXiv:2405.05307, doi: [10.48550/arXiv.2405.05307](https://doi.org/10.48550/arXiv.2405.05307)
- Thorngren, D. P., & Fortney, J. J. 2018, AJ, 155, 214, doi: [10.3847/1538-3881/aaba13](https://doi.org/10.3847/1538-3881/aaba13)
- Thorngren, D. P., Fortney, J. J., Murray-Clay, R. A., & Lopez, E. D. 2016, ApJ, 831, 64, doi: [10.3847/0004-637X/831/1/64](https://doi.org/10.3847/0004-637X/831/1/64)
- Turner, J. D., Griebmeier, J.-M., Zarka, P., Zhang, X., & Mauduit, E. 2024, A&A, 688, A66, doi: [10.1051/0004-6361/202450095](https://doi.org/10.1051/0004-6361/202450095)
- Turner, J. D., Zarka, P., Griebmeier, J.-M., et al. 2021, A&A, 645, A59, doi: [10.1051/0004-6361/201937201](https://doi.org/10.1051/0004-6361/201937201)
- Viganò, D., Sengupta, S., Soriano-Guerrero, C., et al. 2025, A&A submitted
- Wahl, S. M., Hubbard, W. B., Militzer, B., et al. 2017, Geophys. Res. Lett., 44, 4649, doi: [10.1002/2017GL073160](https://doi.org/10.1002/2017GL073160)
- Wazny, M., & Menou, K. 2025, ApJL, 979, L31, doi: [10.3847/2041-8213/ada954](https://doi.org/10.3847/2041-8213/ada954)
- Weiss, L. M., Marcy, G. W., Rowe, J. F., et al. 2013, ApJ, 768, 14, doi: [10.1088/0004-637X/768/1/14](https://doi.org/10.1088/0004-637X/768/1/14)
- Wood, B. E., Müller, H. R., Zank, G. P., Linsky, J. L., & Redfield, S. 2005, ApJL, 628, L143, doi: [10.1086/432716](https://doi.org/10.1086/432716)
- Wood, B. E., Müller, H.-R., Redfield, S., et al. 2021, ApJ, 915, 37, doi: [10.3847/1538-4357/abfda5](https://doi.org/10.3847/1538-4357/abfda5)
- Wu, Y., & Lithwick, Y. 2013, ApJ, 763, 13, doi: [10.1088/0004-637X/763/1/13](https://doi.org/10.1088/0004-637X/763/1/13)
- Yadav, R. K., Gastine, T., Christensen, U. R., & Duarte, L. D. V. 2013, ApJ, 774, 6, doi: [10.1088/0004-637X/774/1/6](https://doi.org/10.1088/0004-637X/774/1/6)
- Yadav, R. K., & Thorngren, D. P. 2017, ApJL, 849, L12, doi: [10.3847/2041-8213/aa93fd](https://doi.org/10.3847/2041-8213/aa93fd)
- Yıldız, M., Çelik Orhan, Z., Örtel, S., & Çakır, T. 2024, MNRAS, 528, 6881, doi: [10.1093/mnras/stae476](https://doi.org/10.1093/mnras/stae476)
- Youdin, A. N., & Mitchell, J. L. 2010, ApJ, 721, 1113, doi: [10.1088/0004-637X/721/2/1113](https://doi.org/10.1088/0004-637X/721/2/1113)
- Zarka, P. 1998, J. Geophys. Res., 103, 20159, doi: [10.1029/98JE01323](https://doi.org/10.1029/98JE01323)
- Zarka, P., Treumann, R. A., Ryabov, B. P., & Ryabov, V. B. 2001, Ap&SS, 277, 293, doi: [10.1023/A:1012221527425](https://doi.org/10.1023/A:1012221527425)
- Zink, J. K., & Howard, A. W. 2023, ApJL, 956, L29, doi: [10.3847/2041-8213/acfdab](https://doi.org/10.3847/2041-8213/acfdab)

APPENDIX

A. ROSSBY NUMBER DEPENDENCE ON STELLAR TYPE

To evaluate the dependence of Ro on stellar type, we use the properties of the specific stars shown in Table 1. Note that, by construction, the evolutionary models are the same but shifted in orbital period, since the relevant parameter is the stellar irradiation, which depends on P_{orb} and stellar mass. The Rossby profiles are instead different, since the Ro definition includes a further P_{orb} dependency. Similarly to Fig. 5, in Fig. 10 we show Ro as a function of planetary depth and orbital period for an M3, K3, and F5 stars. As expected, the more massive the star, the more inflated the planets are, which leads to larger values of Ro , though they remain smaller than 0.1 for the F5 models.

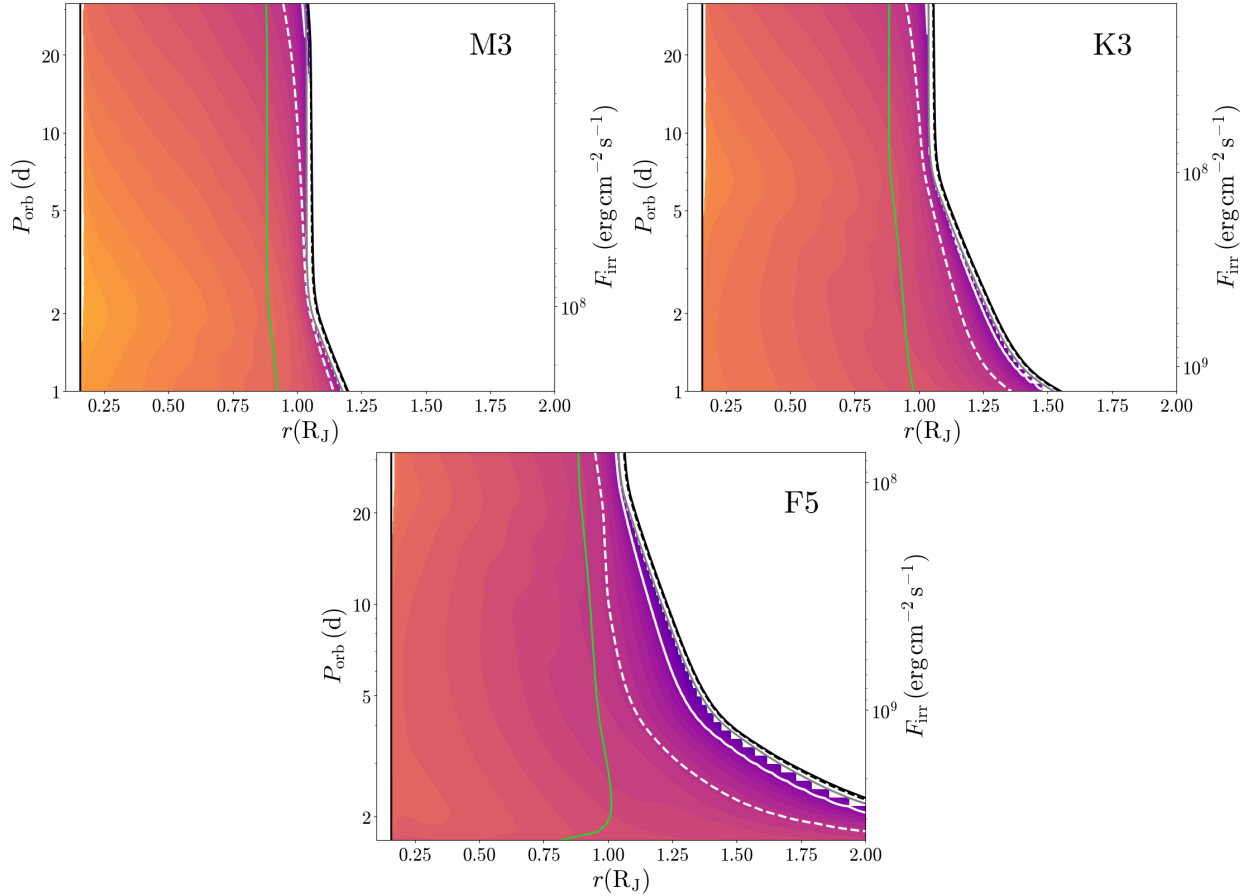


Figure 10. Similar to Fig. 5: Ro as a function of r and a for a $1 M_J$ planet orbiting the different stars shown in Table 1. Only the inflated models with heat injection below the irradiated layer are shown.